

Experimental Observations on Dynamic Response of Selected Transparent Armor Materials

J. W. McCauley, E. Strassburger, P. Patel, B. Paliwal and K. T. Ramesh

ARL-RP-0493

July 2014

A reprint from *Experimental Mechanics*, Vol. 53, no. 1, pp. 3–29, January 2013.

NOTICES

Disclaimers

The findings in this report are not to be construed as an official Department of the Army position unless so designated by other authorized documents.

Citation of manufacturer's or trade names does not constitute an official endorsement or approval of the use thereof.

Destroy this report when it is no longer needed. Do not return it to the originator.

Army Research Laboratory

Aberdeen Proving Ground, MD 21005-5066

ARL-RP-0493**July 2014**

Experimental Observations on Dynamic Response of Selected Transparent Armor Materials

J. W. McCauley and P. Patel
Weapons and Materials Research Directorate, ARL

E. Strassburger
Fraunhofer Institut für Kurzzeitdynamik (EMI)

B. Paliwal and K. T. Ramesh
Johns Hopkins University

A reprint from *Experimental Mechanics*, Vol. 53, no. 1, pp. 3–29, January 2013.

REPORT DOCUMENTATION PAGE				Form Approved OMB No. 0704-0188	
Public reporting burden for this collection of information is estimated to average 1 hour per response, including the time for reviewing instructions, searching existing data sources, gathering and maintaining the data needed, and completing and reviewing the collection information. Send comments regarding this burden estimate or any other aspect of this collection of information, including suggestions for reducing the burden, to Department of Defense, Washington Headquarters Services, Directorate for Information Operations and Reports (0704-0188), 1215 Jefferson Davis Highway, Suite 1204, Arlington, VA 22202-4302. Respondents should be aware that notwithstanding any other provision of law, no person shall be subject to any penalty for failing to comply with a collection of information if it does not display a currently valid OMB control number. PLEASE DO NOT RETURN YOUR FORM TO THE ABOVE ADDRESS.					
1. REPORT DATE (DD-MM-YYYY) July 2014		2. REPORT TYPE Reprint		3. DATES COVERED (From - To) 2006–2012	
4. TITLE AND SUBTITLE Experimental Observations on Dynamic Response of Selected Transparent Armor Materials				5a. CONTRACT NUMBER	
				5b. GRANT NUMBER	
				5c. PROGRAM ELEMENT NUMBER	
6. AUTHOR(S) J. W. McCauley, E. Strassburger, P. Patel, B. Paliwal, and K. T. Ramesh				5d. PROJECT NUMBER	
				5e. TASK NUMBER	
				5f. WORK UNIT NUMBER	
7. PERFORMING ORGANIZATION NAME(S) AND ADDRESS(ES) U.S. Army Research Laboratory ATTN: RDRL-WM Aberdeen Proving Ground, MD 21005-5066				8. PERFORMING ORGANIZATION REPORT NUMBER ARL-RP-0493	
9. SPONSORING/MONITORING AGENCY NAME(S) AND ADDRESS(ES)				10. SPONSOR/MONITOR'S ACRONYM(S)	
				11. SPONSOR/MONITOR'S REPORT NUMBER(S)	
12. DISTRIBUTION/AVAILABILITY STATEMENT Approved for public release; distribution is unlimited.					
13. SUPPLEMENTARY NOTES A reprint from <i>Experimental Mechanics</i> , Vol. 53, no. 1, pp. 3–29, January 2013.					
14. ABSTRACT Structural transparent material systems are critical for many military and civilian applications. Transparent armor systems can consist of a wide variety of glass laminate assemblies with polymeric bonding interfaces and backing as well as the inclusion of polycrystalline ceramic (AlON, spinel) and single crystals (sapphire) as front facing materials. Over the last 20 years as the threats have escalated and become more varied, the challenges for rapidly developing optimized threat specific transparent armor packages have become extremely complex. Ultimate failure of structural ceramics in impact events is a function of the temporal and spatial interaction of the macrostresses at the macro-, micro- and nano-structural scale, including elastic and inelastic (plastic) deformation, crack nucleation, damage evolution and resulting failure from the macro-scale (top down) and/or from the nano-scale (bottom up). In order to accelerate the development of validated design and predictive performance models, a systematic series of experimental investigations have been carried out on various non-crystalline ceramics (glass), single crystal (sapphire) and polycrystalline ceramics (AlON).					
15. SUBJECT TERMS dynamic mechanical tests, glasses, ceramics, AlON, sapphire, high speed photography					
16. SECURITY CLASSIFICATION OF:			17. LIMITATION OF ABSTRACT UU	18. NUMBER OF PAGES 32	19a. NAME OF RESPONSIBLE PERSON J. W. McCauley
a. REPORT Unclassified	b. ABSTRACT Unclassified	c. THIS PAGE Unclassified			19b. TELEPHONE NUMBER (Include area code) 410-306-0711

Experimental Observations on Dynamic Response of Selected Transparent Armor Materials

J.W. McCauley · E. Strassburger ·
P. Patel · B. Paliwal · K.T. Ramesh

Received: 29 March 2012 / Accepted: 18 July 2012 / Published online: 21 August 2012
© Society for Experimental Mechanics (outside the USA) 2012

Abstract Structural transparent material systems are critical for many military and civilian applications. Transparent armor systems can consist of a wide variety of glass laminate assemblies with polymeric bonding interfaces and backing as well as the inclusion of polycrystalline ceramic (AlON, spinel) and single crystals (sapphire) as front facing materials. Over the last 20 years as the threats have escalated and become more varied, the challenges for rapidly developing optimized threat specific transparent armor packages have become extremely complex. Ultimate failure of structural ceramics in impact events is a function of the temporal and spatial interaction of the macrostresses at the macro-, micro- and nano-structural scale, including elastic and inelastic (plastic) deformation, crack nucleation, damage evolution and resulting failure from the macro-scale (top down) and/or from the nano-scale (bottom up). In order to accelerate the development of validated design and predictive performance models, a systematic series of experimental investigations have been carried out on various non-crystalline ceramics (glass), single crystal (sapphire) and polycrystalline ceramics (AlON). The Edge-on Impact (EOI) test coupled with

a high-speed Cranz-Schardin film camera has been extensively used on a variety of monolithic and laminated glasses, AlON and crystallographically controlled sapphire single crystals to visualize and quantify stress wave, crack and damage propagation. A modified Kolsky bar technique instrumented with a high speed digital camera has been utilized in an unconfined and confined test sample mode to examine the dynamic deformation and failure of AlON undergoing uniaxial, high strain rate compression. Real time photography has clearly demonstrated the critical influence of defects and post mortem characterization of fragments resulting from these tests have revealed the influence of micro-deformational twinning and cleavage down to the nano-scale. Finally, a brief summary of work using ultra-high-speed photography of the impact of conventional projectiles on glass and AlON will be presented. These experimental results will be absolutely critical to help evolve and validate existing models used in computer codes to simulate the impact performance of brittle materials.

Keywords Dynamic mechanical tests · Glasses · AlON · Sapphire · High speed photography

J.W. McCauley (✉) · P. Patel
U.S. Army Research Laboratory,
Aberdeen Proving Ground, MD, USA
e-mail: james.w.mccauley.civ@mail.mil

P. Patel
e-mail: parimal.j.patel.civ@mail.mil

E. Strassburger
Fraunhofer Institut für Kurzzeitdynamik (EMI),
Kandern, Germany
e-mail: elmar.Strassburger@emi.fraunhofer.de

B. Paliwal · K.T. Ramesh
Johns Hopkins University,
Baltimore, MD, USA

K.T. Ramesh
e-mail: ramesh@jhu.edu

Introduction

Structural transparent material systems are critical for many military and civilian applications. They span the range from the use of transparent armor systems for military personnel, ground vehicles and aircraft, dignitary protection, automobile windows to special architectural windows. Also, these same or similar materials are used for missile domes, IR windows, hyper-hemispherical domes, laser windows, semiconductor processing applications, and scanner windows (Point of Sale (POS) windows). The challenge for transparent armor materials is to provide protection, some structural integrity and visible light transparency at the same time, all



for an affordable cost. They have to provide protection, not only against a variety of projectiles, but also against fragments, road and other debris and blast waves from detonations. These systems (Fig. 1) typically consist of several layers of glass with polymer interlayers and backing, which is still mainly an empirical process [1]. Their performance is influenced by many parameters, including number, thickness and type of the glass layers, thickness and type of the bonding layers and the polymer backing; a variety of different techniques are required for systematic optimization. In addition, the use of single crystals (sapphire) or transparent polycrystalline ceramics (AlON, spinel) front faces adds an additional level of complexity, but provides less weight and thickness and protection against more severe threats.

Experiences over the last 20 years have clearly demonstrated the criticality of transparent armor in many military systems [1–3]. As the threats have escalated and become more varied, the challenges for rapidly developing optimized, threat specific transparent armor packages have become extremely complex. Ultimate failure/penetration of structural ceramics and glass in impact events is a function of the temporal and spatial interaction of the macro-stresses at the macro-, micro- and nano-structural scale. This includes determining the mechanisms involved in elastic and inelastic (plastic) deformation, damage nucleation and evolution and resulting failure from the macro-scale (top down) and from the nano-scale (bottom up) for the various materials. The impact event can be divided into two main parts: projectile deformation and erosion and target material damage and failure. Simplistically, the target material failure/penetration is comprised of the initiation of penetration, followed by projectile penetration through fragmented striking ply material. Subsequent layers in the line of sight may not be fractured, but the stress state has changed from the

pre-impact condition. The relationship between the projectile/target interaction coupled with intermediate and backing materials is complex. Various computational models and codes have been developed to simulate various impact events, but many of these are extrapolations from metal behavior and involve material specific adjustable parameters which are not physics based [4]. Many exclude defects, micro-cracking/cleavage, deformational twinning, ceramic-specific plasticity and failure mechanisms, among other physics based phenomena. Inelastic deformation mechanisms of polycrystalline structural ceramics in impact events, although seemingly important as energy absorption mechanisms, have not been sufficiently characterized. In addition, the velocities of cracks and the damage zone are very important. The experimental determination of many of these associated phenomena is critical for the validation of the various computational models and codes. For the highly complex laminate systems, validated models can expedite the design optimization much more rapidly than empirical techniques alone.

This review will briefly summarize experimental work carried out over the past several years in collaborations with the Fraunhofer-Institut für Kurzzeitdynamik, Ernst-Mach-Institut (EMI), Efringen-Kirchen, Germany, Johns Hopkins, Rutgers, The Pennsylvania State and Tohoku Universities (Sendai, Japan) on AlON, sapphire, and various glasses/laminates.

Background

It will be important to have a basic understanding of some simple aspects of a dynamic impact event to appreciate the various results presented in this review article. Table 1

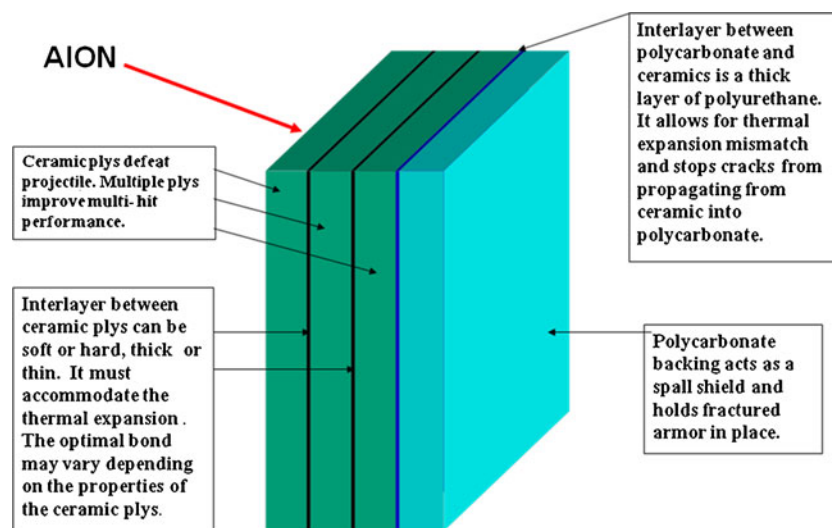


Fig. 1 Schematic of a laminated transparent armor system, modified from [1]

Table 1 Simplified differences between quasi-static and dynamic stress environments

	Quasi-static bend bar stress environment	Ballistic stress environment
Stressed Volume	Typically Small ~12 mm ³	Huge 15–20,000 mm ³
Rate and defects	Largest Defect	Many Defects Tail of Distribution
Cracks	Single crack	Many cracks Massive failure
Rate and micro- mechanisms	<ul style="list-style-type: none"> • Partial dislocations • Slip • Toughness • Others 	<ul style="list-style-type: none"> • Deformational twinning • Amorphization • Bulk Plasticity • Micro-cleavage, others
Stress Characteristics	• Gradual rise to failure	<ul style="list-style-type: none"> • Mixed stress states: compression, tension (spall), shear (Shear increasing) • Hertzian • Shock wave “conditions” material • Super stress condition

summarizes some key differences between conventional quasi-static mechanical testing and a dynamic impact event on a large sample. In the context of this manuscript the strain rate assumed for quasi-static mechanical testing is on the order of 10^{-3} to 10^{-2} s⁻¹ and “dynamic” testing is in the range of 10^2 to 10^4 s⁻¹. Basically, the stressed volume in most impact events can be much larger than conventional quasi-static testing resulting in the activation of a much larger distribution of defects, microstructural inhomogeneities, and other stress concentration regions. Sequences of shock waves are generated consisting of a surface wave (Rayleigh wave), compression/longitudinal wave (dilatational, push or p wave) and a shear (transverse, shake or s wave) wave. Assuming an harmonic normal load in the impact event, the total energy in the shock waves is roughly partitioned as follows: 67 % in the Rayleigh (R) wave, 26 % in the shear (S) wave and 7 % in the compression (C) wave [5]. This is schematically represented in Fig. 2. The relative velocities are as follows: $V_C > V_S > V_R$. Excluding major surface imperfections, the key waves for the bulk material are the compression and shear waves. The compression wave can densify the material in both a reversible and irreversible way and begin to “activate” defects and condition the microstructure. The shear wave, with significantly more energy, can then begin to grow, propagate and coalesce cracks into a damage front. The impact event can result in an impact stress/pressure that is significantly larger than the compressive strength of the material, thus “over-stressing” the material. The impact pressure (P) can be approximated using the following formula:

$$P = (V_p)((Z_p)(Z_{\text{targ}})/(Z_p + Z_{\text{targ}}))$$

where V_p = impactor velocity; Z_p = projectile impedance; Z_{targ} = target impedance

$$Z = \text{acoustic impedance} = \rho c_L = (\rho E)^{\frac{1}{2}}$$

where ρ is density, c_L is longitudinal sound wave velocity and E is the elastic modulus.

For example, for a steel projectile impacting an AlON plate these would be the calculated approximate pressures:

$$\text{AlON: } \rho_{\text{AlON}} = 3.67 \text{ g/cm}^3, c_L = 10.250 \text{ km/s,}$$

$$\text{Steel: } \rho_{\text{steel}} = 7.85 \text{ g/cm}^3, c_L = 5.1 \text{ km/s}$$

Impact pressures:

- V_p of 200 m/s in AlON ≈ 3.88 GPa.
- V_p of 900 m/s in AlON ≈ 17.44 GPa

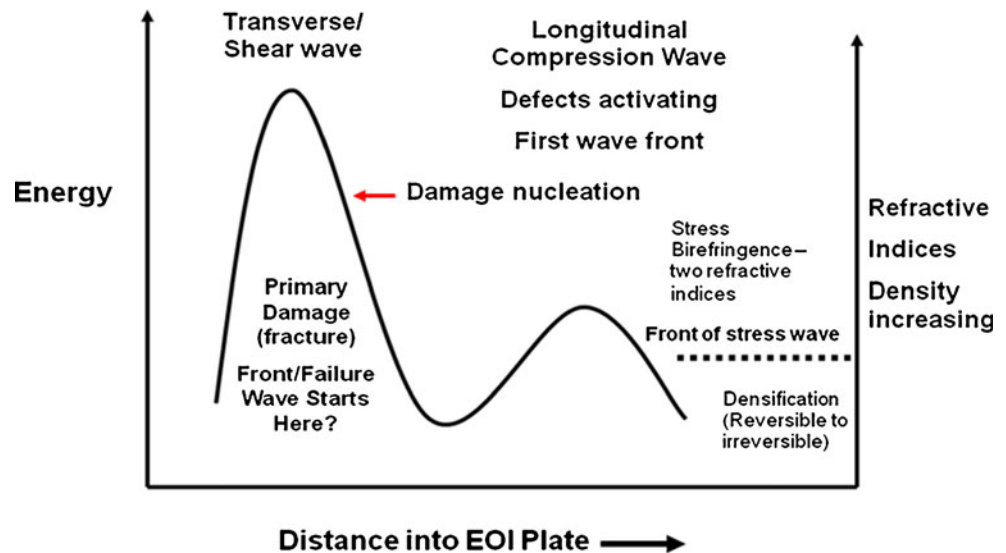
Typical impact pressure in impact events like the Edge-on Impact test can be on the order of 4–30 GPa depending on the impactor material, its velocity and the target material. The typical quasi-static and dynamic compressive strength for AlON can be between 2 and 4 GPa, so for most EOI impacts the compressive strength is exceeded.

Mechanical Testing

Edge-On Impact (EOI) Tests

The EOI test method coupled with a high-speed Craz-Schardin camera, with frame rates up to 10^7 fps, developed at the Fraunhofer Institute for High-Speed Dynamics, Ernst-Mach-Institute (EMI) has been used to visualize damage propagation and dynamic fracture in glass and many opaque structural ceramics in a back reflection technique [6–8]. The transparency of AlON has allowed for observations in a transmission, shadowgraph mode. Two different optical configurations were employed. A regular transmitted light shadowgraph set-up was used to observe damage nucleation and propagation and a modified configuration, where the sample plates were placed between crossed polarizers and the photoelastic effect (polariscope technique) was utilized to visualize the stress waves. Pairs of impact tests at approximately equivalent velocities were carried out in transmitted unpolarized (shadowgraphs) and crossed polarized light. Figure 3(a) illustrates a schematic of the EOI test with the added crossed polarizers and Fig. 3(b) is a photo of the actual set up with some of the authors. Figure 4 illustrates an exploded view of the impactor/sample interaction. In some tests, both horizontal (perpendicular to plate) and vertical (perpendicular to long edge) photographs were obtained. This method allows for the real time observation of various phenomena including: nucleation of cracks, number, density, influence of defects and monitoring and

Fig. 2 Hypothetical dynamic shock stress waves/energy profiles in an Edge-on Impact (EOI) test



velocity determination of damage fronts and stress waves using the photoelastic effect in crossed polarizers.

Both steel cylinders and sabot spherical impactors (Fig. 5(a, b)) have been used at velocities from 125 m/s–950 m/s on $100 \times 100 \times 10$ mm plates, which roughly corresponds to strain rates of 10^2 to 10^3 s $^{-1}$.

- Steel Cylinder (7.85 g/cc)
 - Diameter 30 mm
 - Length 23 mm
 - Total Mass 54 g
- Spherical Steel Impactor
 - Steel ball
 - Diameter 15.87 mm
 - Mass 16.2 g

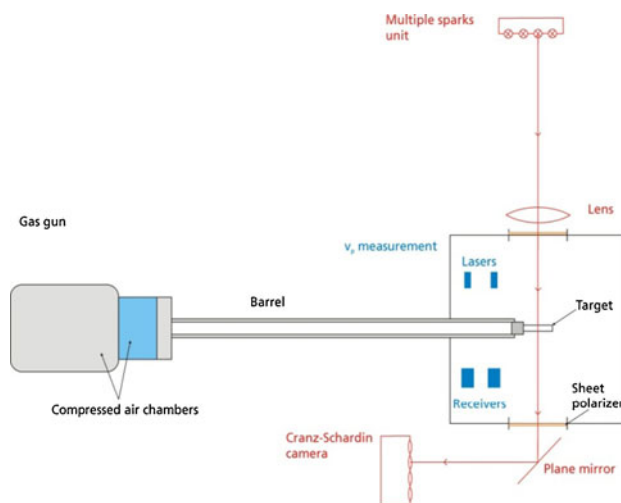
- Sabot: (polycarbonate)

Diameter 30 mm
 Length 27.5 mm (sabot plus steel sphere)
 Mass 22.9 g
 Total Mass=39.1 g

The data collected from the EOI test consists of a series of 20 photographs as a function of time, typically at 0.25–2 μ s intervals. Detailed graphs are then created plotting crack, damage, and compression and shear stress wave velocities.

Nomenclature for EOI tests

Since two different methods (shadowgraphs, crossed polarizers) were employed for the visualization of wave and damage propagation, where not only the stress waves appear



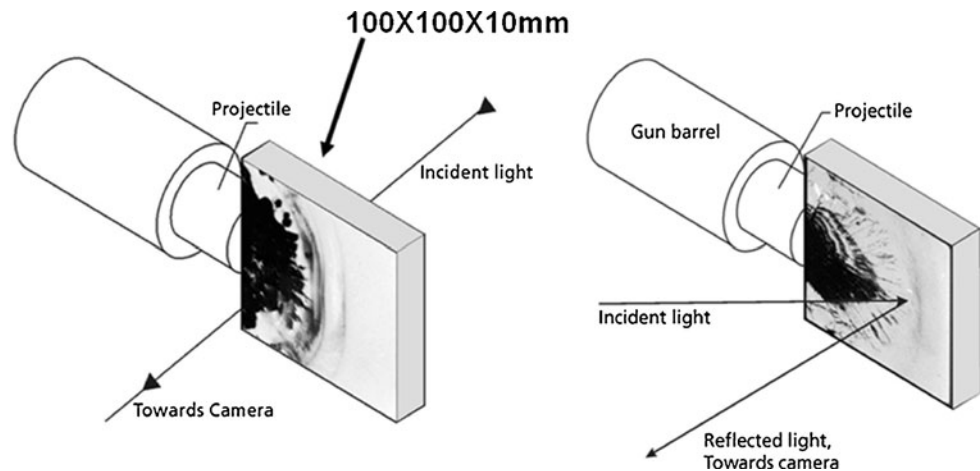
(a) Schematic of EOI



(b) Photograph of experimental setup

Fig. 3 EOI test set-up with Cranz-Schardin camera

Fig. 4 EOI transmitted light (shadowgraph) and reflected light configurations



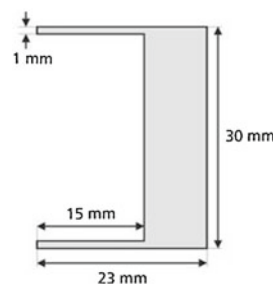
in different forms, but also different types of fracture can be distinguished, it is necessary to clarify the designations of the various phenomena [8].

Cracks, Fracture and Damage Figure 6(a) illustrates typical damage patterns observed using the shadowgraph technique with soda-lime (float) glass at ~ 200 m/s impact velocity, while Fig. 6(b) illustrates the typical damage pattern in Starphire™ (PPG Industries), a high-purity soda-lime glass, at an impact velocity of ~ 400 m/s. Figure 6(c) shows the damage pattern in AlON, a transparent, polycrystalline ceramic at about the same impact velocity. Based on our conceptual understanding of the progression of the shock waves in the EOI plate as shown in Fig. 2, it is our conclusion that the crack centers ahead of the primary fracture front in Fig. 6(a) are nucleated either by the interaction of the compression wave or the shear wave with the defects in the material, depending on the amplitude of the waves. In the examples of Fig. 6(a, b) crack nucleation and growth was initiated by the shear waves mainly, whereas in case of Figure 6(c) nucleation by the longitudinal wave was dominant. These isolated cracks centers can have a significant influence on the morphology and progression of the primary fracture fronts. In these figures the primary fracture zone/front is the best approximation of the coherent area of undifferentiated, massive cracking. The damage front

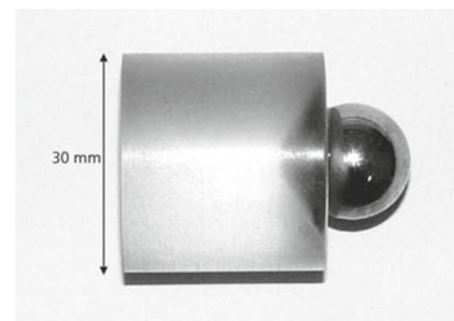
is a similar circular approximation of the cracks/crack fingers ahead of the primary fracture front. In the following sections, damage velocity refers to the velocity of the primary, coherent fracture zone when no isolated crack centers can be distinguished. When the time and position of the appearance of isolated crack centers can be observed, the damage velocity is defined as the slope of the regression straight line through the leading nucleation points. The dashed straight line through the nucleation sites in Fig. 11, which represents the distance-time plot for the test depicted in Fig. 6(c), shows an example. Crack velocity refers to the velocity of the expanding isolated cracks. The coherent fracture front in Fig. 6(c) is a circular approximation of the cracks/crack fingers at the head of the damage zone. In Fig. 6(b) the damage front is a circular approximation of the tips of the cracks from the primary fracture front. The distinction of these different fracture/damage zones/fronTS is not clear in some cases, especially if there are many isolated cracks initiated in front of the main damage zone. In the following sections, damage velocity refers to the velocity of the primary fracture zone, whereas the crack velocity refers to the velocity of the expanding isolated cracks, unless otherwise noted.

Waves The two different optical techniques employed exhibit different sensitivities with respect to the stress level

Fig. 5 Cylindrical and sabot spherical impactors



(a) Schematic of cylindrical steel projectile



(b) Photograph of spherical steel projectile with sabot.

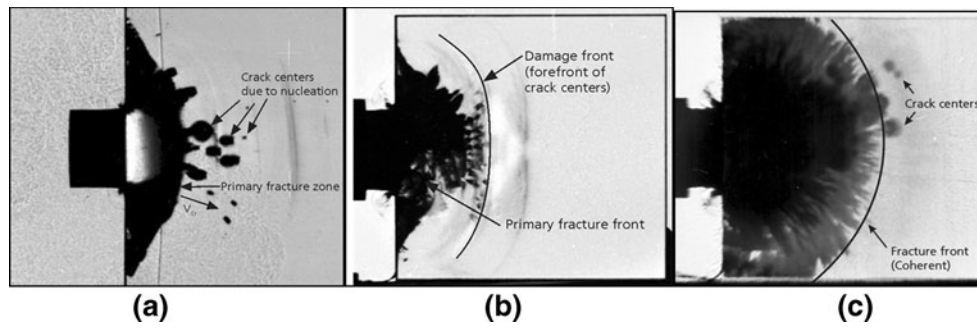


Fig. 6 Damage patterns obtained using the shadowgraph technique without crossed polarizers. (a) Typical damage pattern in float glass at $v_p \approx 200$ m/s, (b) Typical damage pattern with Starphire™ glass at $v_p \approx 400$ m/s; see Fig. 7 for the crossed polarizers image of the stress wave, (c) Typical damage pattern in AION at $v_p \approx 400$ m/s; the coherent fracture front is a circular approximation of the cracks/crack fingers at the head of the damage zone

that can be visualized. In a shadowgraph image, the light intensity depends on the second spatial derivative $\partial^2 n / \partial x^2$ of the refractive index, whereas in the crossed polarizers setup, the intensity of the transmitted light depends on the photo-elastic properties of the material. Therefore, it is possible that the first visible wave front in the shadowgraph configuration appears at a different position than the forefront of the stress wave, visible in the crossed polarizers setup. Both techniques can visualize different parts of the same stress wave. This is illustrated in Fig. 7, which shows the shadowgraph and the corresponding crossed polarizers photograph of a Starphire™ sample at 8.7 μ s after impact.

The width of the compression stress wave can be estimated from the length of the impactor and the longitudinal wave speed in the impactor and target material. When the impactor hits the target, a wave is generated not only in the target, but also in the impactor. The maximum length of the stress pulse is given by the time the wave needs to travel once through the impactor and back. The thickness of the solid cylindrical part of the impactor was 8 mm. With a longitudinal wave speed of 5,100 m/s in steel, this yields the following stress pulse length:

$$\Delta t_{\text{stress}} \approx 2 \cdot \frac{8 \text{ mm}}{5.1 \frac{\text{mm}}{\mu\text{s}}} = 3.1 \mu\text{s} \quad (1)$$

Release waves from the edges of the projectile are neglected in this estimate. The longitudinal wave velocity in Starphire™ glass is $\approx 5,800$ m/s. Therefore, the maximum spatial width of the stress wave in the target can be calculated as follows:

$$\Delta s_{\text{stress}} \approx 3.1 \mu\text{s} \cdot 5.8 \frac{\text{mm}}{\mu\text{s}} \approx 18 \text{ mm} \quad (2)$$

The formation of the second wave front is caused by the geometry of the specimens and is due to the initiation and superposition of waves, generated at the side surfaces of the specimens. The distance to the first wave front depends on the thickness and Poisson's ratio. In Fig. 7 the forefront of

the stress wave is that front part of the wave that initiates photoelastic birefringence and the 1st wave front is approximately the stress wave maximum.

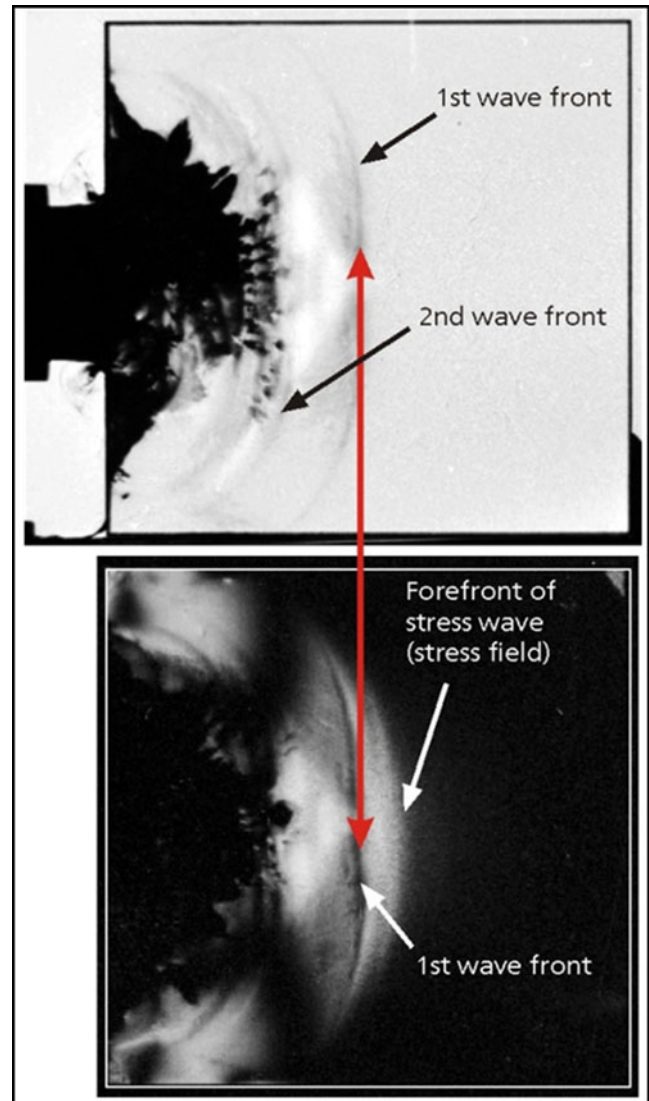


Fig. 7 Shadowgraph (top) and corresponding crossed polarizers photograph (bottom) of Starphire™ specimen, 8.7 μ s after impact at ≈ 400 m/s

Kolsky Bar Tests (Split Hopkinson Pressure Bar)

Ultra-high-speed photography with an inter-frame time of 1 μs and an exposure time of 100 ns, has been used to observe the dynamic failure of transparent AlON undergoing uniaxial, high strain rate compression (10^3 s^{-1}) in a Johns Hopkins University modified Kolsky bar with confinement of about 400 MPa (Fig. 8(a, b)); unconfined samples do not have the anvil arrangement. The high-speed photographs are correlated in time with direct measurements of the stresses in the sample. Prismatic sample sizes were on the order of $2 \times 4 \times 5 \text{ mm}$. Numerical simulations of the confinement test arrangements were performed using ABAQUS / STANDARD. In order to determine the level of confinement applied to the specimen, it was necessary to calibrate the torque applied to the bolts against the compressive force that is transmitted through the specimen. A cuboidal calibration specimen made from Ti – 6Al – 4V alloy was used for this purpose. References 9 and 10 describe the details of these tests.

Results on Crystalline Ceramic Materials

AlON EOI Tests

AlON is isostructural with magnesium aluminate spinel (MgAl_2O_4) having a cubic crystal structure (Fd3m) that can be processed to transparency in a polycrystalline microstructure [9]. The atomic structures/crystal chemistry of AlON and spinel are slightly different as follows (stoichiometry of full unit cell):



\square = a cation vacancy at the six-fold (octahedral) site;

Al in both four-fold (tetrahedral) and six-fold coordination;



Mg in four-fold coordination and Al in six-fold coordination.

The grain size of the AlON (ALON™ from Surmet Corporation, Burlington, MA) material varies from 150 to 250 μm on average (Fig. 9). The density is typically 3.67 g/cm^3 , but will vary slightly depending on the composition and porosity. The range of grain sizes for available spinel materials is much greater, varying from about 0.5 μm of the IKTS (Fraunhofer- Institut für Keramische Technologien und Systeme, Dresden, Germany) [10,11] to bi-modal materials of large grains in a fine grain matrix. Results from quasi-static and dynamic mechanical tests on polycrystalline spinel can be found in references [12,13]. A report detailing a comprehensive characterization and evaluation of the IKTS transparent fine-grained spinels is currently in preparation [14]. In addition, a major investigation of the fragmentation of the various spinels and AlON in a ballistic impact test arrangement has been carried out with preliminary results already published [15] and more comprehensive results to be presented at the 27th International Symposium on Ballistics [16].

For the first time the EOI test was used to visualize internal damage evolution in a polycrystalline structural ceramic. Recently, a version of an Edge-on Impact test has been carried out on a polycrystalline spinel by Haney and Subhash [17]. Transparent polycrystalline AlON specimens measuring $100 \times 100 \times 10 \text{ mm}$ were impacted using steel solid cylinder and sabotaged sphere impactors with velocities ranging from 270 to 925 m/s. Pairs of impact tests at approximately equivalent velocities were carried out in transmitted unpolarized (shadowgraphs) and crossed polarized light. A typical series of shadowgraphs and crossed polarized light photographs are illustrated in Fig. 10; the impactor is visible on the left. Figure 10(a) is a series conducted at about 380 m/s and Fig. 10(b) illustrates two series at about 820 and 925 m/s. Most of the EOI tests were carried out at velocities of about 400 m/s or lower using a more controllable gas gun arrangement; velocities greater than about 400 m/s required a powder gun, where the velocities were more difficult to control. Stress wave and damage velocities were determined as well as the nucleation of crack centers ahead of the apparent fracture front [18,19].

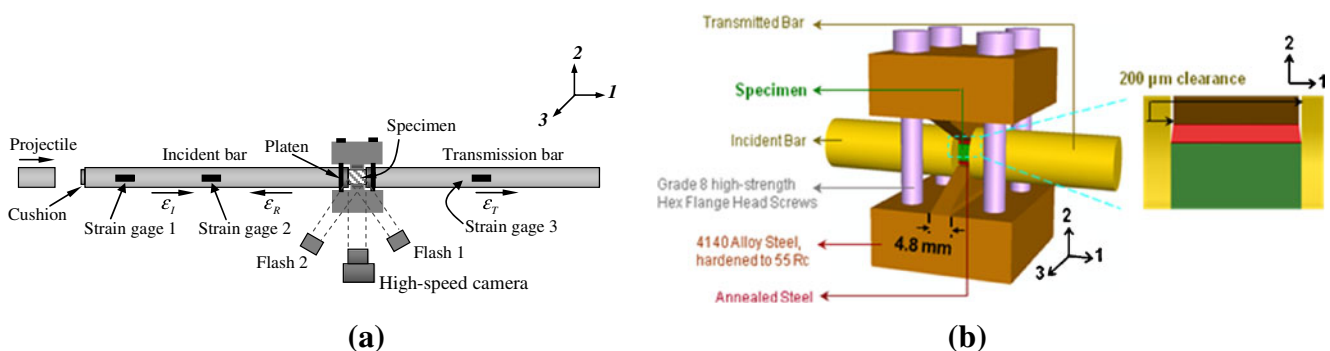


Fig. 8 Johns Hopkins Kolsky Bar schematics [7,8]: (a) Kolsky bar and sample; (b) confinement arrangement

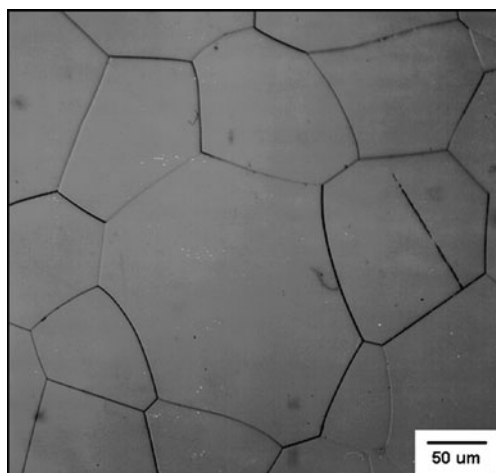


Fig. 9 Typical microstructure of AlON

There are several features visible on these photographs. On the shadowgraphs distinct growing darkened regions can be seen in rows 1 and 3 that probably reflect a massively fractured damage zone that could be referred to as a failure wave. In addition, the shadowgraphs at 6.7, 7.7 and 8.7 μs , show the nucleation of clearly visible crack centers ahead of the damage front, probably from bulk defects, which are similar to those seen in Fig. 6(a) on glass. The observation of nucleation of crack centers ahead of the damage front is an important observation for both glasses and polycrystalline ceramics. Though the materials are transparent, this does not mean that they do not have any bulk defects. There are defects (stress concentration/intensity regions) that can nucleate and grow cracks that have been observed in both EOI tests and the Kolsky tests. In the crossed polarized light photographs, in rows 2 and 4, a band of visible light is apparent. This is the result of stress induced birefringence (photoelasticity) due to the passing of the compression stress wave; the velocity of this wave should be very close to the longitudinal acoustic wave velocity (c_L) in AlON.

Figure 11 exhibits distance-time plots of compression wave and damage/fracture and isolated crack propagation for AlON at a nominal impact velocity of 380 m/s. Wave propagation could only be observed through crossed polarizers. A wave front velocity of 9,367 m/s was determined, which is consistent with the sound velocity of AlON (c_L) at 10.1–10.3 km/s. The coherent damage/fracture front initiated at the impacted edge of the specimen propagated at an average velocity of 8,381 m/s. Ahead of this front several crack centers (see Fig. 6(c)) could be observed and plotted on Fig. 11. The nucleation sites were extrapolated and linear regression of this data (black diamonds, dashed line) resulted in a velocity of 9,156 m/s. The wave and fracture velocities were determined by linear regression of the distance-time data ($y=a_0+a_1t$). The standard deviations s_{a1} of the slopes of the straight lines are given as error intervals

for the damage velocities and wave velocities and were determined according to the following equation:

$$s_{a1}^2 = \frac{\sum_{i=1}^n (y_i - a_0 - a_1 t)^2}{n-2} \frac{n}{n \sum t^2 - (\sum t)^2} \quad (2)$$

For example, for the velocity data in Fig. 11, using (equation (2)), the following standard deviations can be calculated:

- Nucleation site velocity = 9,156 m/s with a standard deviation of 886 m/s (~10 %)
- Fracture front velocity = 8,381 m/s with a standard deviation of 182 m/s (~2.2 %)
- Wave velocity = 9,367 m/s with a standard deviation of 113 m/s (~1.2 %)

In other sections of this review the same methodology can be used to calculate the velocities and the related standard deviations, however, in general the percent standard deviations will be very close to these values for the respective velocities.

The damage velocities of AlON and other ceramics as a function of impactor velocity are plotted in Fig. 12 [19]. First, it should be noted that other than AlON, all of the other velocities were determined in reflection on opaque ceramics. It appears that the damage velocities of AlON, Al_2O_3 and WC do not increase significantly from about 200–900 m/s. On the other hand, the damage velocities of TiB_2 and SiC-B seem to increase continuously for these same impactor velocities. In the velocity range of the AlON tests there was no indication of a change in slope reflective of a deformation or damage mechanism change. As can be seen on Fig. 10(a, b), there does not appear to be any clear damage morphology differences between the low and high impactor velocities; of course only very careful post mortem characterization of the resulting fragments would verify this conclusion. One possible explanation of the velocity differences between the two sets of data could be the role of inelastic or plastic deformation mechanisms operative in AlON, Al_2O_3 and WC that slow the crack/damage propagation, whereas the SiC-B and TiB_2 material may behave in a brittle, primarily elastic way. B_4C , however, showed a change in slope at about 600 m/s which could be the result of stress induced nano-amorphization, but this would have to be confirmed by post mortem high resolution transmission electron microscopy [20]. The change in slope at about 200 m/s may be due to a combination of experimental issues and a dwell penetration transition. Finally, one must proceed with caution in trying to relate these damage velocities to the compression or the shear waves exclusively. Even though the relative energies (ratio) in the two waves remain fairly constant, the energy in the compression and shear waves

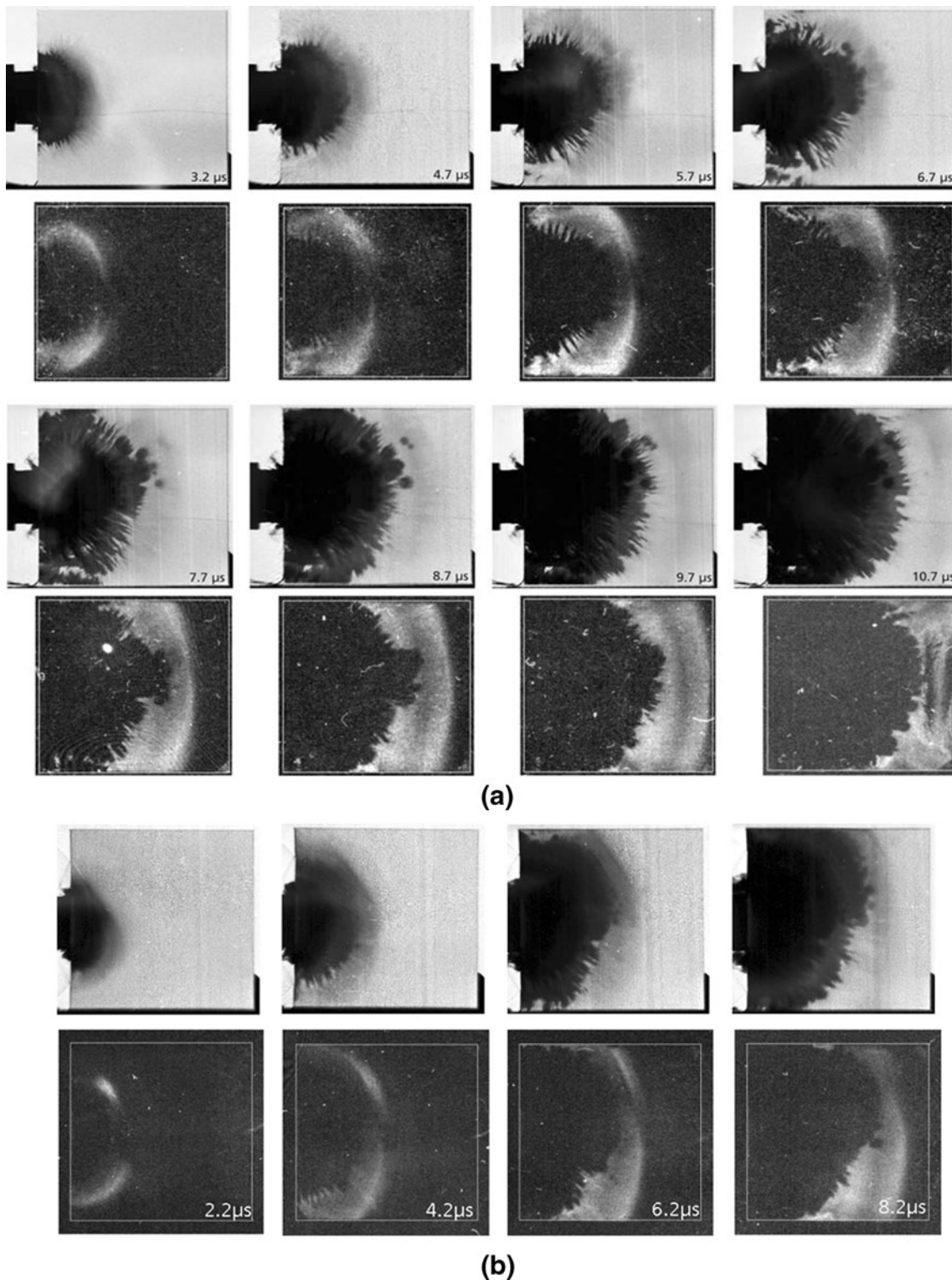
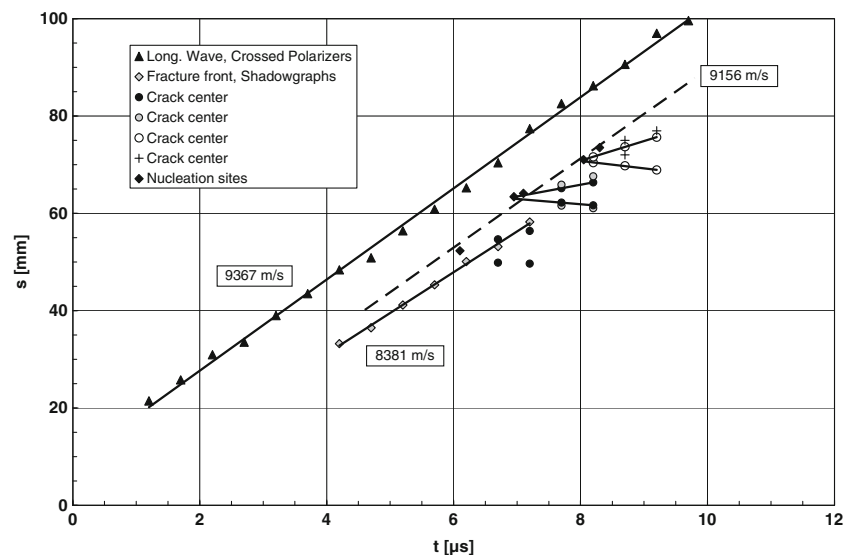


Fig. 10 (a) Series of alternating shadowgraphs (row 1(*top*) and 3) and crossed polarized light photographs (rows 2 and 4) of AION impacted by a solid steel cylinder at a velocity ≈ 380 m/s. (b) Series of shadowgraphs (*top row*) and crossed polarized light photographs of AION impacted at 820 (*top*) and 925 m/s (*bottom*)

increase significantly with impactor velocity, to the point that the compression wave has enough energy to increase the damage velocity in purely or predominantly elastic materials.

Since previous work at EMI on opaque ceramics [7] was done in a reflected light mode, an additional test was carried out at 380 m/s nominal impact velocity in a reflected light

Fig. 11 Distance-time plot of longitudinal wave and damage propagation of tests in Fig 10(a); s is the distance into the AION plate



set-up with an AION specimen that was coated with silver on one surface. These tests allowed us to distinguish between surface damage and damage in the interior of the specimens. Photographs at 5.2 and 8.7 μs of coated AION tested at an impact velocity of 397 m/s in the reflected light test configuration are shown in Fig. 13(b); shadowgraphs and a crossed polarized light photograph are shown in Fig. 13(a) for ease of comparison. The damage front detail and observation of the cracks nucleating from internal defects are obvious improvements and highlight the use of transparent ceramics as model materials to understand behavior of polycrystalline opaque ceramics.

Figure 14 illustrates the differences between the morphology of the damage fronts from impacting with a spherical *versus* a solid cylinder impactor [21]. This could be due to the difference in weight between the sphere at 39.1 g compared to the cylinder at 54 g and the resulting deposited energy at the same velocity or the stress distribution below

the two impactors. Grinfield, et al. [22] used a thermodynamic based hypothesis to explain the sphere impact results.

Figures 15(b, c) and 16 illustrate fracture surfaces of the fragment shown in Fig. 15(a) that came from a confined EOI test. It is clear that besides intergranular fracture, there is a significant intragranular microcleavage mechanism operative down to the nano-scale, as illustrated in Fig. 16. Whether the cleavage is preceded by micro-deformational twinning is still unknown, but, in any case, this may be considered as a plasticity mechanism prior to catastrophic macro-cracking/failure. LaSalvia and McCauley [23] have previously discussed concepts of inelastic deformation mechanisms and damage in structural ceramics subjected to high-velocity impact. Capturing these mechanisms in existing dynamic brittle ceramic computer codes is a significant modeling challenge.

Computational simulations have been carried out [24] of the elastic wave propagation within the AION EOI as shown in Fig. 17. A computational model was constructed using ABAQUS Explicit to simulate the elastic wave propagation within the experiment. Since the experiment provides snapshots of the deformation and the stress state at specific times, the simulation results provide snapshots at identical times for comparison. The computational model was fully 3-dimensional, so that longitudinal and shear waves, surface waves and plate waves could all be captured. The computational results show that the observed propagation of the longitudinal wave in the specimen is a result of the impact, as well as the subsequent edge unloading. The simulations also show that the damaged region observed in the experiments corresponds essentially to the region that has observed shear as a result of the wave propagation (Fig. 17). The character of the damage itself, and its kinetics, cannot, of course, be captured with this elastic simulation. However, the correlation of the damage propagation speed with

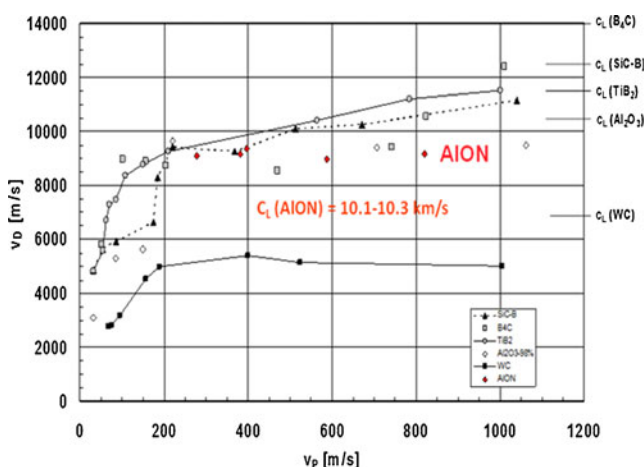


Fig. 12 Damage velocities (v_D) of ceramics at various EOI (cylinder) impact velocities (v_P) [19]

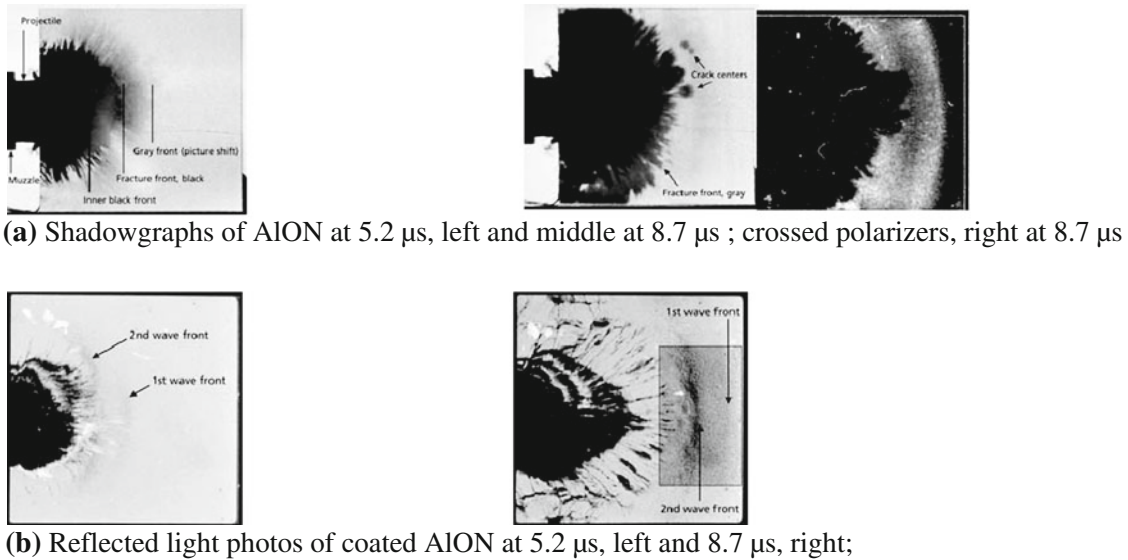


Fig. 13 Shadowgraphs and reflected light, coated photograph of AION at $v_p \approx 397$ m/s

the shear information is an interesting observation. As implied in Fig. 2 the compression wave can begin to “activate/nucleate” cracks from existing defects (stress intensity/concentration regions) which will intensify the passing stress to critical levels, which will then begin to grow extensively with the passage of the shear wave as can be seen in Fig. 6 in both glass and AION. The passing stress has exceeded the failure stress of the defect free material causing the massive fracture zone/damage front to form and propagate. As mentioned previously, however, there is the possibility of

inelastic/plastic deformation mechanisms operative in the crack process zone, such as those shown in Figs. 15 and 16, that could significantly affect the propagation velocity of the various cracks and failed damage zone material, which is not captured in this simulation.

AION Kolsky Tests

High-speed photography has been used to observe the dynamic failure of transparent polycrystalline AION undergoing uniaxial, high strain rate compression with a

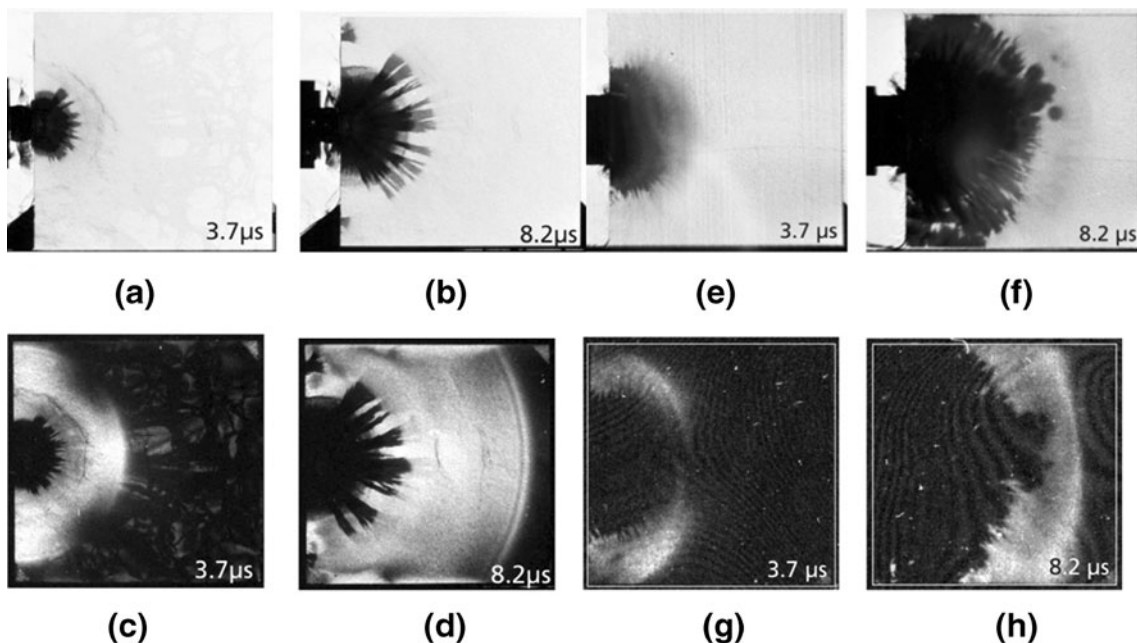


Fig. 14 Photographs of AION impacted with spheres and cylinders. (a) and (b): Sphere impactor in shadowgraphs; (c) and (d): in crossed polarized light; 3.7 and 8.2 μs , (e) and (f): Cylinder impactor in shadowgraphs; (g) and (h): crossed polarized light; 3.7 and 8.2 μs

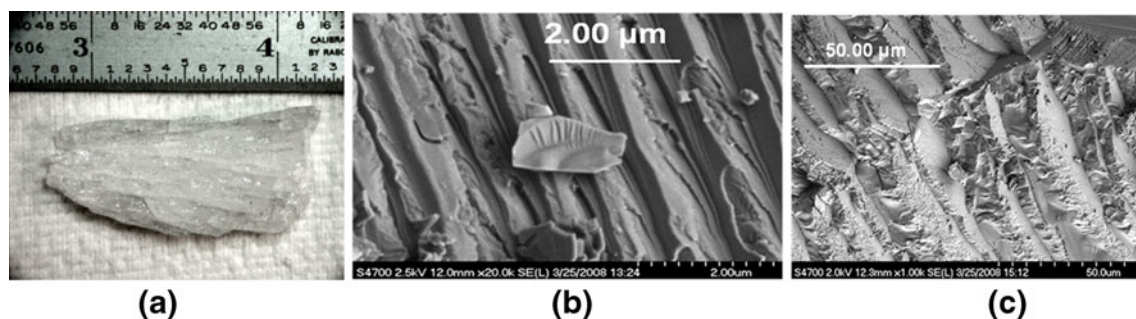


Fig. 15 (a) AION fragment from an EOI test, (b) and (c) SEM photographs of fragment in Fig 15(a)

modified compression Kolsky bar technique, as described above. The high-speed photographs are correlated in time with direct measurements of the stresses in the specimen. The dynamic activation, growth and coalescence of cracks and resulting damage zones from spatially separated internal defects has been directly observed and correlated to the macroscopic loss of load-carrying capacity and ultimate catastrophic failure.

Figure 18 illustrates an example of a modified Kolsky bar test presented in a series of high-speed photographs, together with the corresponding stress history, indicating the times at which each exposure was made; a loading rate of 155 MPa/μs was used. [25] The numbered points on the stress history correspond to the times at which the eight photographs were taken. Since the flashes are on the same side of the specimen as the camera, only reflected light enters the camera, and the transparent specimen is initially dark. The stress-time curve shows that the peak stress achieved is 3.76 GPa. A total of eight photographs were taken. In frame 4 there are no observable cracks. However, in frame 5 a small cluster of cracks can be seen. As the stress increases in the next frames (6–8), new spatially separated

cracks are formed and the original cracks begin to coalesce, which will lead to ultimate failure. Careful characterization of the fragments revealed the presence of carbonaceous defects (Fig. 19) in the rubble, possibly the stress concentration sources for the formation of the cracks that were observed.

Another series of tests were carried out using a uniaxial confinement technique described above [26]. Figure 20 illustrates one other example of an unconfined test along with a confined test. The differences are readily apparent. The maximum stress increases from about 3.5 to 4.5 GPa and a noticeable change in slope in the confined test appears. It is our conclusion that this is indicative of the initiation of a plasticity mechanism in the AION material. High resolution TEM, shown in Fig. 20, revealed the presence of microcleavage similar to what was observed in the EOI fragment analysis. The confinement seems to suppress crack formation, increase the maximum load carrying stress, allowing the nano/micro cleavage to be activated. The series of photographs from the confined test do not exhibit the formation of noticeable cracks, but a “mist like” zone that propagates smoothly through the material.

As discussed previously, the ultimate failure of structural ceramics in impact events is a function of the temporal and spatial interaction of the macro-stresses at the macro-, micro- and nano-structural scale, including elastic and inelastic (plastic) deformation, crack nucleation, damage evolution and resulting failure from the macro-scale (top down) and/or from the nano-scale (bottom up). So it is very important to identify the operative deformation and failure mechanisms. From the EOI and Kolsky bar mechanical tests it is clear that the presence of inclusions (defects) in AION can nucleate cracks, but that the suppression of crack growth from these defects by the imposition of a confining stress will result in the activation of apparent inelastic deformation mechanisms. In related quasi-static nanoindentation and Hertzian indentation investigations on AION, a variety of deformation mechanisms have been identified that could lead to

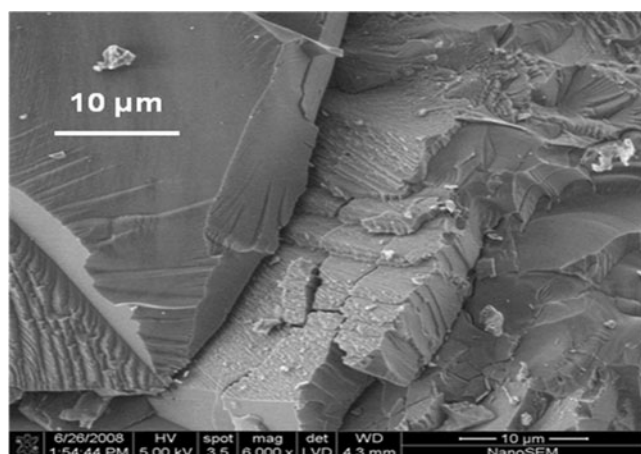
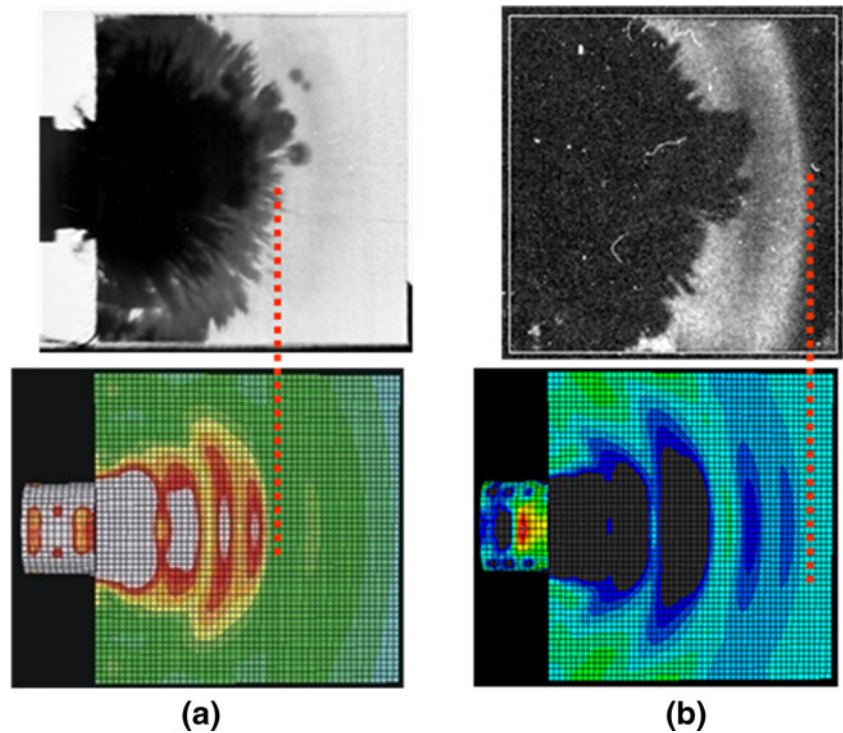


Fig. 16 SEM photograph of an AION fragment showing microcleavage down to the nano-scale

Fig. 17 Comparison of FEA Analysis with EoI Experimental Results on AION at $8.7 \mu\text{s}$ and about 400 m/s ; a. top is a shadowgraph and bottom is the fully 3-D ABAQUS Explicit simulation of the shear dominant von Mises stress and b. top is the crossed polarized light photo and bottom is the fully 3-D ABAQUS Explicit simulation of the S_{11} principal axis stress compression wave



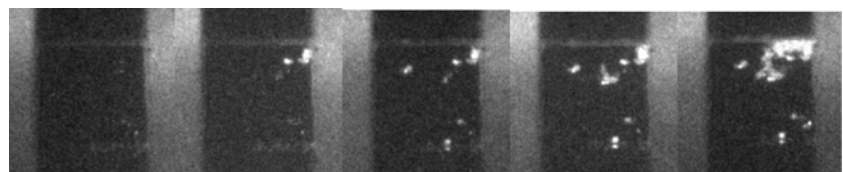
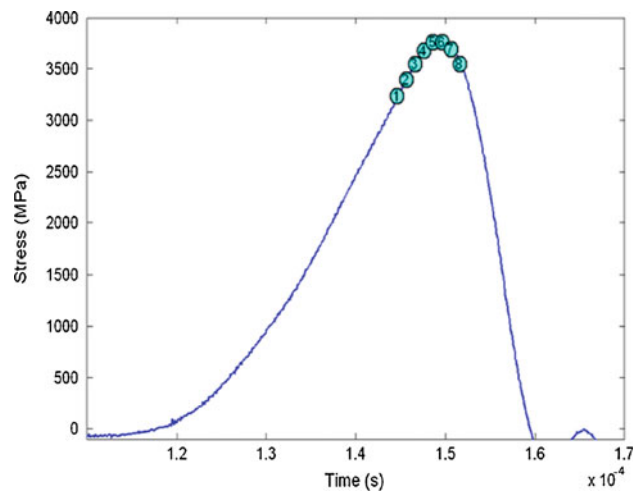
inelastic deformation prior to catastrophic failure in dynamic impact events [27–29].

Sapphire Single Crystal EOI Tests

In previous work with controlled plate impact tests on polycrystalline alumina (Al_2O_3), it was determined that the

response below the Hugoniot Elastic Limit (HEL) is dominated by intergranular failure, while above it by predominantly microdeformational twinning plasticity [30–32]. In addition, recent elegant work using quasi-static and dynamic indentation on sapphire single crystals by Haney and Subhash [33,34] clearly demonstrated the importance of cleavage. As a result of the plate impact work [30–32] it was decided that more

Fig. 18 AION Kolsky bar high speed photography illustrating nucleation of cracks in AION at defects: inter-frame time = $1 \mu\text{s}$, exposure time = 100 ns



Frame 4

Frame 8

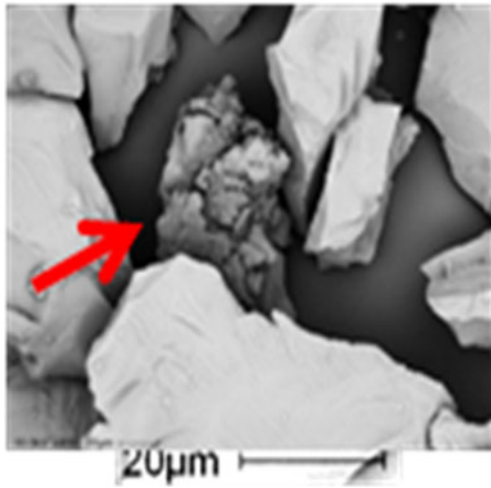


Fig. 19 SEM photo of fragments from a typical unconfined test highlighting a carbonaceous defect

controlled dynamic EOI tests on crystallographically controlled single crystal sapphire impacts might shed additional light on the operative mechanisms in the individual alumina grains.

Monolithic single crystal sapphire plates ($100 \times 100 \times 10$ mm), from GT Crystal Systems, Inc., Salem, MA, in crystallographically controlled directions, have been impacted at about 400 m/s with both steel solid cylinders and spheres. The plates were impacted as follows:

- Orientation #1: impact direction parallel to a-axis; 100×100 mm surface is (0001)
- Orientation #2: impact direction parallel to a-axis; 100×100 mm surface is r-plane

- Orientation #3: impact direction parallel to c-axis; 100×100 mm surface is a-plane
- Orientation #4: impact direction is perpendicular to c-axis; 100×100 mm surface is a-plane
- Orientation #5: impact direction is perpendicular to r-plane; r-plane parallel to impact edge

Winkler and then Senf and Winkler [35,36] were the first to use the EOI test to study sapphire. Recent investigations expanded on this work by impacting the sapphire in controlled crystallographic directions [37].

A selection of eight high-speed photographs from the impact of a steel sphere on the edge of a sapphire specimen at 453 m/s, in orientation #1, where the impact was parallel to the a-axis (100×100 mm surface is (0001)), is presented in Fig. 21. Also, illustrated in this composite figure is a photograph of the actual plate before impact, with the crystallographic directions indicated and a conoscopic (viewed in crossed polarizers) interference figure photograph; note that the optical figure is not quite centered, meaning that the c-axis is not quite perpendicular to the large surface. The first cracks, possibly along prismatic (m-plane) cleavage planes, appeared immediately after impact, cutting a cone with an angle of about 120° into the specimen (fractures A, B). After $2.7 \mu\text{s}$ a third main fracture was visible, propagating straight in the impact direction (C). About eight microseconds later cracks branched off the cone cracks at an angle of about 60° , growing in the impact direction. C cracks also branched off from the central fracture at an angle of about 55° . The distance-time histories of the different fractures are shown in Fig. 22. All fractures propagated at average velocities of between 4,590 m/s and 4,934 m/s; assuming a 2 %

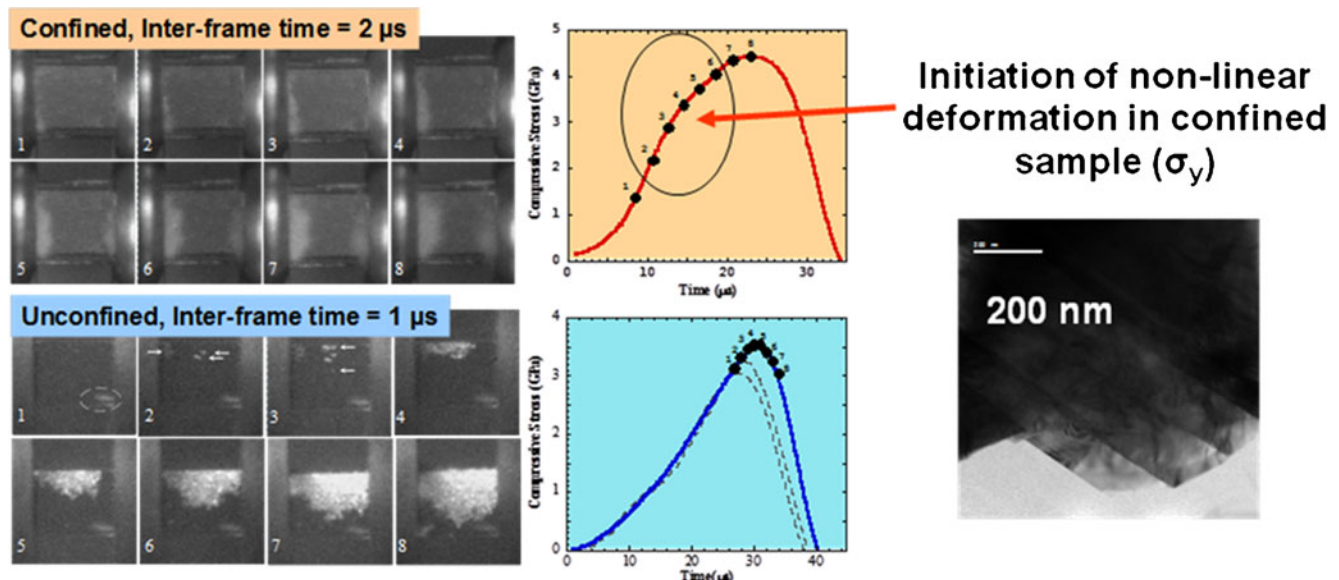


Fig. 20 Ultra-high-speed photographs of the dynamic (10^3 s^{-1}) failure of AION with (top) & without confinement (400 MPa); dynamic compression along the horizontal axis. Exposure times are 100 ns. TEM photograph courtesy of Professor Mingwei Chen, Tohoku University

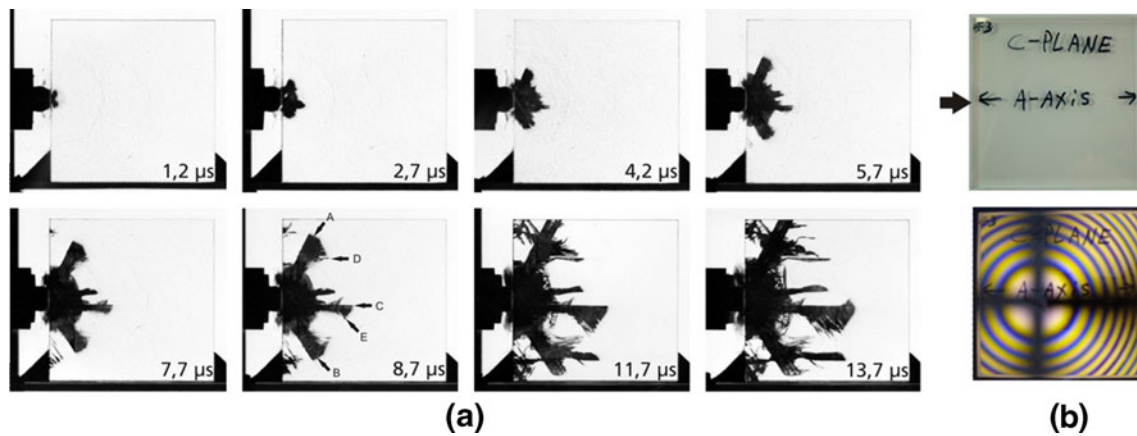


Fig. 21 Sphere impact on sapphire: c-axis perpendicular to plate, impact parallel to a-axis; orientation #1. (a) Selection of 8 high-speed shadowgraphs; (b) Plane light photograph of specimen before impact, illustrating the impact configuration (top) and conoscopic (viewed in crossed polars) interference figure photograph – note that the optical figure is not quite centered, meaning that the c-axis is not quite perpendicular to the a-axis plane

standard deviation, cracks B, C, and D were basically the same velocity. The error for fracture E was on the order of about 10 %, which would also mean that all of the cracks traveled at approximately the same velocity. For the sake of clarity in the distance-time plots, arbitrary offsets were added to the coordinates of different fractures.

Figure 23 shows a selection of 8 high-speed photographs of sapphire in the same orientation as in Fig. 21, but impacted with a steel cylinder. The distance-time history and velocities for the test shown in Fig. 23 are shown in Fig. 24. The photograph in Fig. 23 at 1.2 μ s after impact shows that crack formation starts along the edge of the projectile, where shear stresses are dominant. After 3 μ s, a dense fracture zone has evolved ahead of the projectile, developing a nearly semi-circular shape. A velocity of 11,451 m/s was determined for the longitudinal wave from the shadowgraphs; this value is very close to the range determined by Winey and Gupta [38]. The fracture front ahead of the impactor propagated at an average constant velocity of 8,434 m/s. Cracks A and C grew at average speeds between 5,200 m/s and 5,700 m/s, whereas fracture B in the center propagated at about the same speed as the fracture front

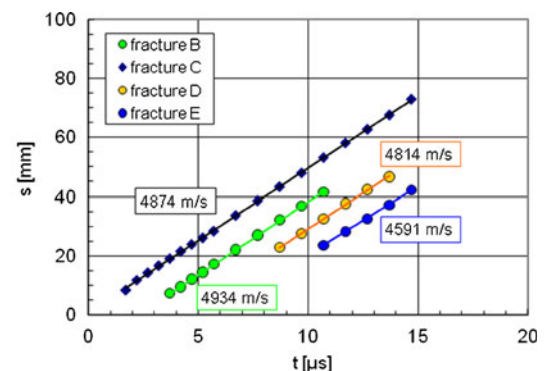
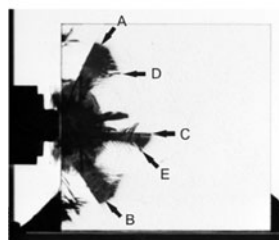
($v_{\text{fracture}}=8,137$ m/s). In contrast to the impact of a steel sphere on sapphire, where crack propagation occurred along apparent crystallographic directions/cleavage planes, the fracture pattern due to impact of a steel cylinder exhibited many similarities to the fracture patterns observed with the polycrystalline transparent ceramic ALON.

A comparison between steel sphere impacts on ALON and sapphire is shown in Fig. 25 at about the same impactor velocity and at comparable times after impact; the differences are obvious. It is clear that for this set of experimental conditions the control of fracture by the cleavage planes in sapphire seems to be apparent.

Figure 26 illustrates SEM photomicrographs of sapphire fracture surfaces impacted at 457 m/s with a sphere in orientation #3 with impact parallel to c-axis, and the 100 \times 100 mm surface parallel to the a-plane. Cleavage controlled fractures from the nano- to the micro-scale are apparent.

Figure 27 exhibits shadowgraphs of sapphire impacted with a sabot steel sphere in the five different orientations. For these experimental conditions, the available cleavage planes play a dominant role in controlling the fracture front when the energy available is not enough to

Fig. 22 Distance-time history of fracture propagation of various cracks in Fig. 21



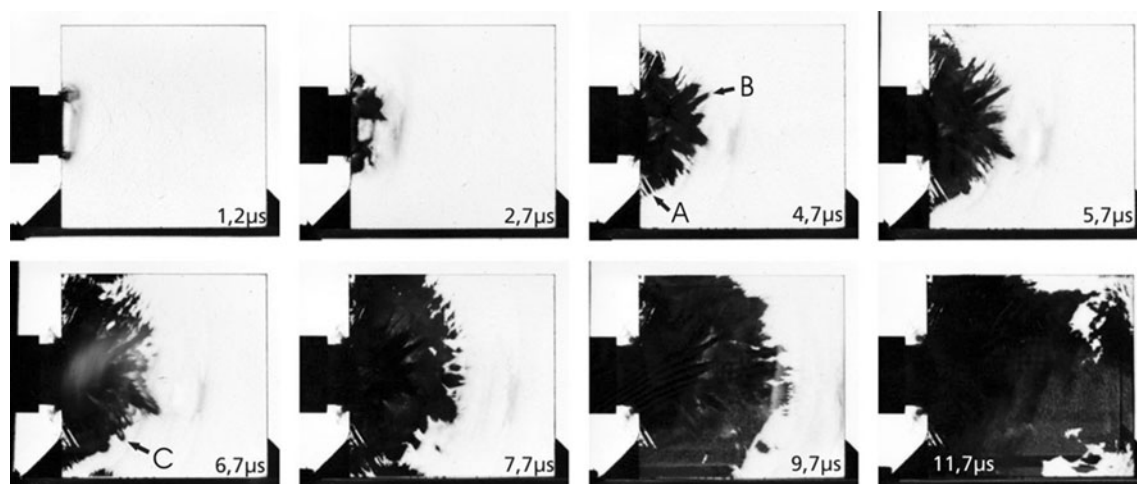


Fig. 23 Cylinder impact on sapphire; c-axis perpendicular to plate- impact parallel to a-axis; same orientation #1 as in Fig. 21

propagate an undifferentiated damage zone. Bradt [39,40] has reviewed the relevant properties, experimental and theoretical energies for the three cleavage planes for sapphire; these are presented in Table 2. The predominant cleavage planes are as follows: the c-plane (0001) basal plane; the r-plane ($10\bar{1}2$) rhombohedral plane and the m-plane ($10\bar{1}0$) prismatic plane. The theoretical surface energies (γ_s) at about 6.5 J/m^2 are almost equal for all three cleavage planes. However, the experimental K_{IC} toughness and cleavage energies are as follows: (0001) = $4.54 \text{ MPa m}^{1/2}$ and 21.54 J/m^2 ; ($10\bar{1}2$) = $2.38 \text{ MPa m}^{1/2}$ and 6.45 J/m^2 and ($10\bar{1}0$) = $3.14 \text{ MPa m}^{1/2}$ and 11.43 J/m^2 . This suggests that the energy to propagate a cleavage crack is most difficult along the (0001), followed by the ($10\bar{1}0$) and ($10\bar{1}2$) planes. It is well known that rhombohedral cleavage predominates in sapphire [41]. Clayton [45] has recently reviewed continuum modeling theory for sapphire.

It is the author's view that the morphology of the damage front will be controlled by a competition

between the available impact energy to create a massive undifferentiated damage front with the energy to have the damage controlled by the available properly oriented cleavage planes. Although the shadowgraphs in Fig. 23 exhibit some cracks at the front of the damage zone, in the author's opinion these are not cleavage controlled and are very similar to those in polycrystalline AlON. For certain levels of energy deposition, the critical resolved shear stress (Schmid factor), which is a function of the angle between the loading direction and the cleavage plane, will control the ease of formation of cleavage controlled cracks/damage or undifferentiated damage zones. Therefore, in some sapphire plate orientations damage will be dominated by cleavage and not in others.

In addition, it should be noted that the mass of the solid cylinder impactor (54 g) compared to the sphere impactor (39 g) means that at the same velocity the energy deposited by the solid cylinder is more than that of the sphere. In the solid cylinder case, since the available energy is higher than the sphere deposited energy, the energy to propagate an undifferentiated massive damage front has been exceeded and therefore, the available cleavage planes do not dominate the damage front morphology. Another argument could be made that the geometries of the stress fields in the EOI plate from the sphere impact and the solid cylinder impact might also have significant influence on the dominance of the cleavage controlled compared to the undifferentiated damage front as suggested for AlON in the photographs of Fig. 14, but at this point, this has not been determined conclusively.

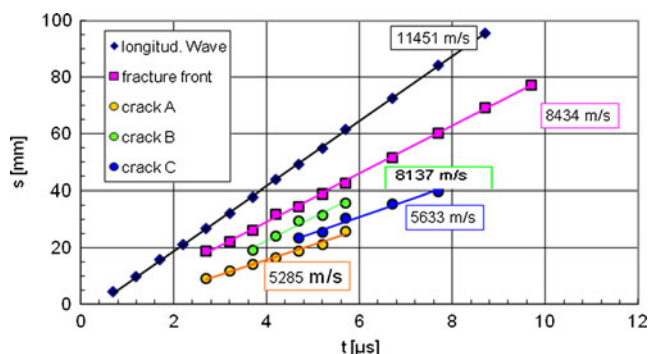
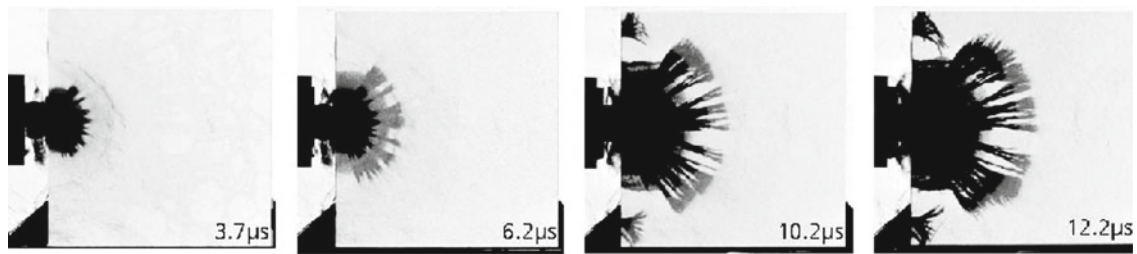


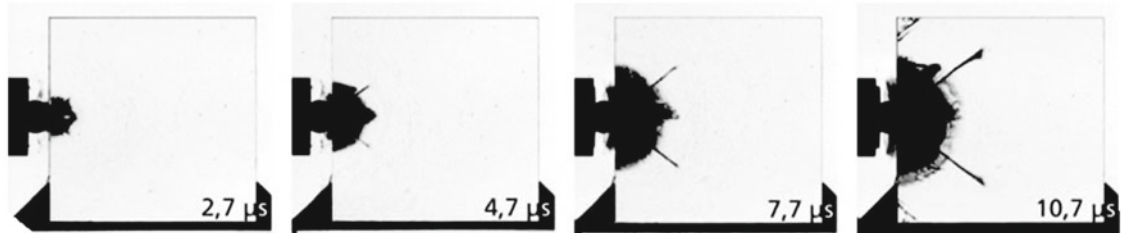
Fig. 24 Distance-time history of fracture propagation of various cracks in Fig. 23

EOI Results on Monolithic Glass and Glass Laminates

Extensive EOI tests were also performed on a series of glass and glass laminates. Selected results from this work will be presented here [8,21,24,46–48].



(a) Steel Sphere on polycrystalline AlON; impact velocity = 429 m/s



(b) Steel sphere impact at 457 m/s on sapphire; orientation #2 – 100X100 mm surface is r-plane, impact parallel to the a-axis

Fig. 25 Comparison of EOI Impact at about 450 m/s on sapphire and polycrystalline AlON

Monolithic Glass

Figure 28(a) illustrates a selection of two shadowgraphs (top) and corresponding crossed polarizers photographs (bottom) of a baseline test with Starphire™ glass (PPG Industries), impacted by a steel sphere impactor at

440 m/s, and Fig. 28(b) shows similar photographs of Starphire™ impacted by a steel cylinder at 390 m/s. The shadowgraphs in the former exhibit a crack front growing from the impacted edge of the plate, whereas only one crack center is visible close to the upper edge of the specimen. Both the longitudinal and the transverse stress

Fig. 26 SEM photomicrographs of sapphire fracture surface impacted at 457 m/s with a sphere in orientation #3; impact parallel to c-axis, 100×100 mm surface parallel to a-plane; courtesy of Dr. Buyang Cao, Johns Hopkins University

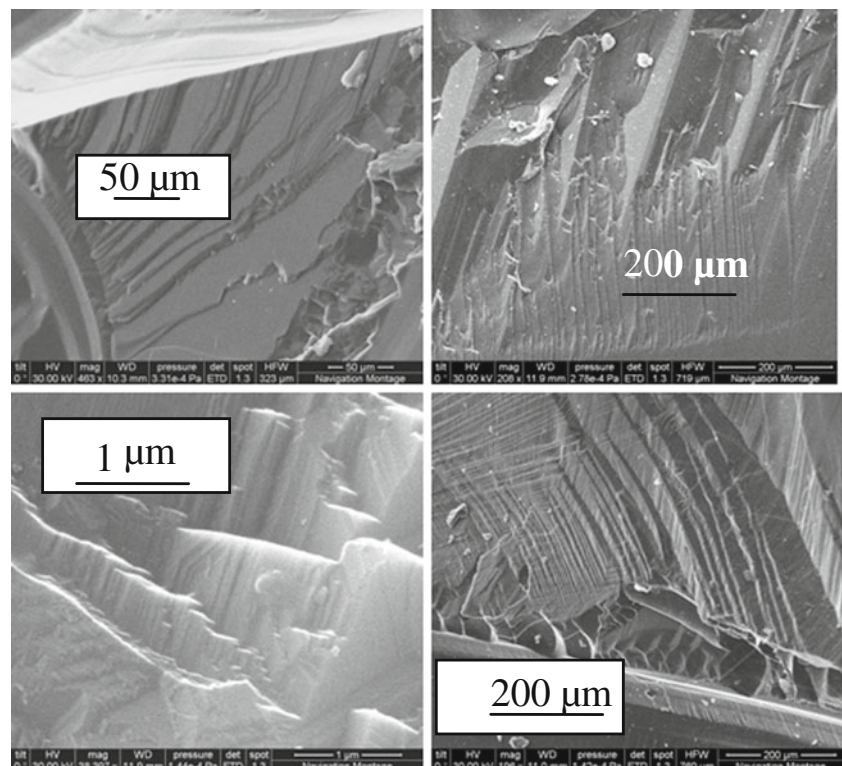
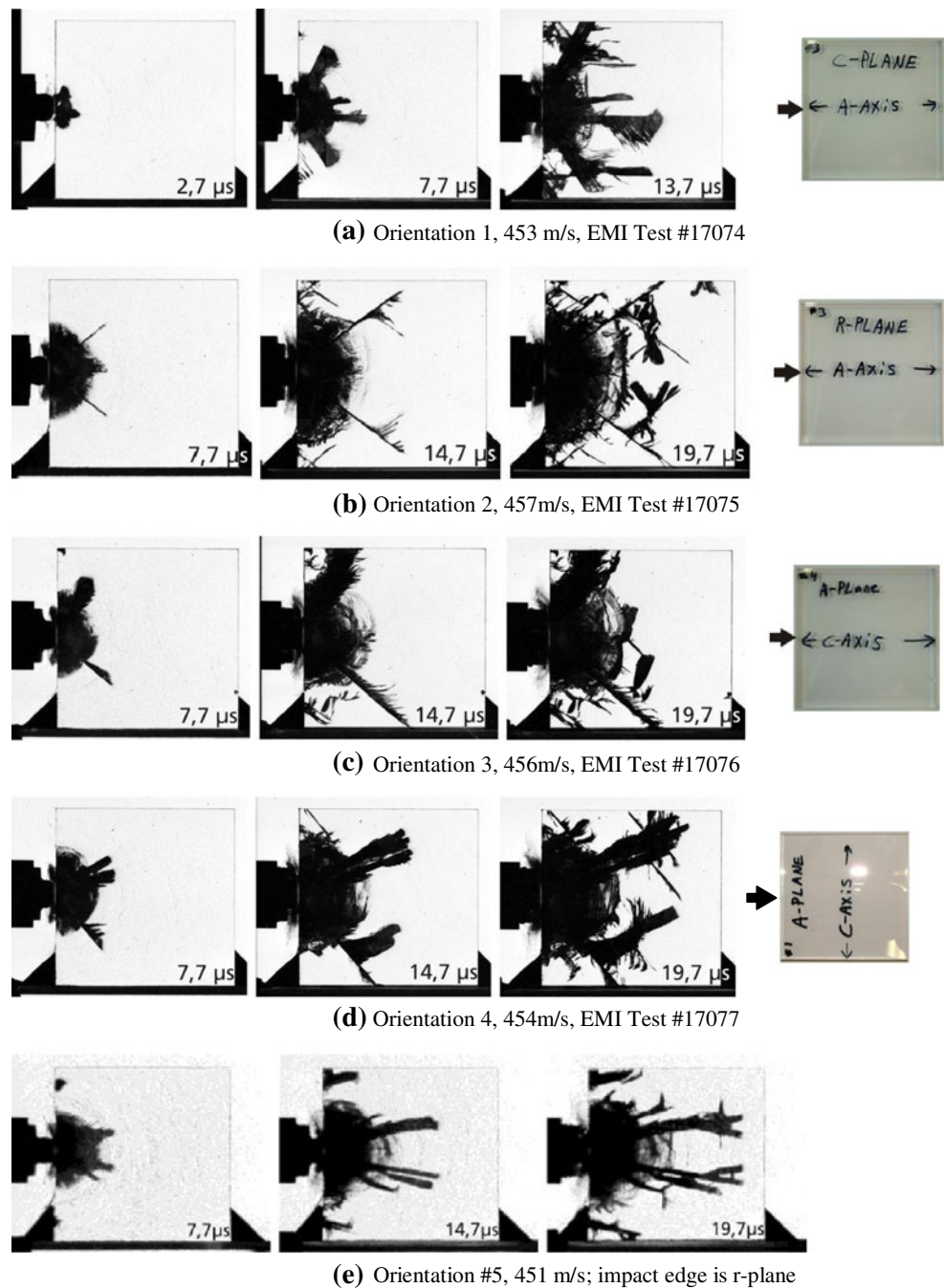


Fig. 27 Shadowgraph analysis of damage and crack morphologies from Sphere EOI Impact in five crystallographic orientations



waves are visible in the crossed polarizers photographs. Release waves due to reflections at the upper and lower edge are also apparent. Recall that damage appears dark on the shadowgraphs and the zones with stress birefringence are exhibited as bright zones in the crossed polarizers photographs.

Figure 28(b) illustrates a selection of two shadowgraphs along with the corresponding crossed polarizers photographs of the baseline tests with the cylindrical impactor. A coherent damage zone is growing from the impacted edge, preceded by a zone with separated crack centers,

initiated by the compression stress waves. This seeming discrepancy can be explained by the different sensitivities that the different optical techniques employed exhibit with respect to the stress level that can be visualized. Recall that in a shadowgraph image the light intensity depends on the second spatial derivative $\partial^2 n / \partial x^2$ of the refractive index, whereas in the crossed polarizers set-up the intensity of the transmitted light depends on the photoelastic/stress birefringence effect. The distance-time histories of the stress waves and the damage propagation are depicted in Fig. 29. Different types of cracks are generated and different fracture

Table 2 Sapphire experimental and theoretical cleavage energies

Plane structural indices	Shappel cleavability ^a	E GPa	K _{IC} MPa m ^{1/2}	Cleavage ^b J/m ²	γ_s J/m ² T	γ_s J/m ² M	γ_s J/m ² H
C(0001)	9.5	465	4.54	21.54	6.5	5.9	4.8
R (10T2)	12.4	440	2.38	6.45	6.4	5.6	4.8
M (10T0)	10.2	430	3.14	11.43	6.9	6.5	–

^a Higher values represent easier cleavage [41]^b experimental values from Bradt [39] and Iwasa and Bradt [40]

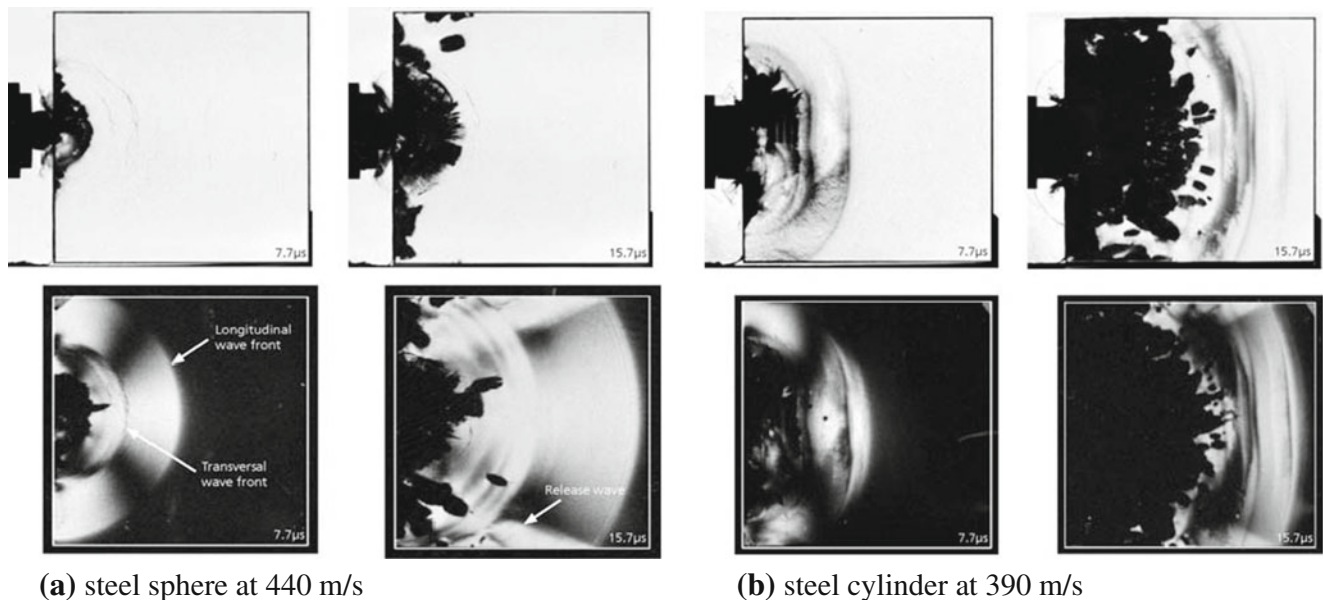
T=Tasker [43], M=Mackrodt [42], H=Hartman [44]; authors initials; theoretical values from (T), (M), (H)

velocities can be observed at one impact velocity in one specimen. Therefore, it is necessary to distinguish between the velocity of single, continuously growing cracks and crack fronts. The term damage velocity is used here to denote the velocity of the fastest fracture which was observed in the material. In order to determine the damage velocity the distances of fracture tips and/or the fracture front are measured and plotted *versus* time. Linear regression of the data delivers fracture and fracture front velocities. Table 3 shows a compilation of crack and damage velocities of two types of glass, fused silica, a glass ceramic, a polycrystalline transparent ceramic (AION) and cleavage cracks in sapphire. In each of the ceramics damage velocity is a function of impact velocity. The damage velocities approach the longitudinal wave velocity c_L at high loadings/impact velocities (see Fig. 12). Therefore, damage velocities are compared for a constant impact velocity of about 400 m/s in Table 3. The growth of four

arbitrarily chosen crack centers at the front of the damage zone were also analyzed; the slope of a straight line through the nucleation sites was 3,269 m/s, which means, that the damage velocity is close to the transverse wave velocity. This is in agreement with our previous FEA modeling on AION discussed above.

Glass Laminates

The influence of a polyurethane (PU) bonding layer on wave and damage propagation in a variety of glass laminates was examined with cylindrical impactors. Four pairs of tests were conducted on Starphire™ laminates consisting of two glass plates, 50×100×9.5 mm, bonded together with PU in the following thicknesses: 0.64, 1.27, 2.54 and 5.08 mm. Figure 30 illustrates a comparison of wave and damage propagation in Starphire™ laminates, with bonding layers of thickness 0.64, 2.54 and 5.08 mm; the impact velocity was 380 ± 5 m/s in all tests. The upper line of photographs shows the shadowgraphs, while the corresponding crossed polarizers photographs are presented in the lower line of photographs; Fig. 30 illustrates the laminates at 10.7 μ s and Fig. 31 at 23.7 μ s after impact. The shadowgraphs at 10.7 μ s exhibit a coherent damage front in the first glass layer growing from the impacted edge through the nucleation of crack centers, initiated by the longitudinal stress wave. At that time, no damage appears in the second glass layer (right part of specimen). The crossed polarizers photographs clearly show that the first longitudinal stress wave has not yet crossed the 5.08 mm PU interlayer, whereas the stress wave is clearly visible in the right half of the specimens with the 0.64 mm PU interlayer.

**Fig. 28** Selection of two shadowgraphs (*top*) and crossed polarizers photographs (*bottom*) from impact on Starphire™ glass

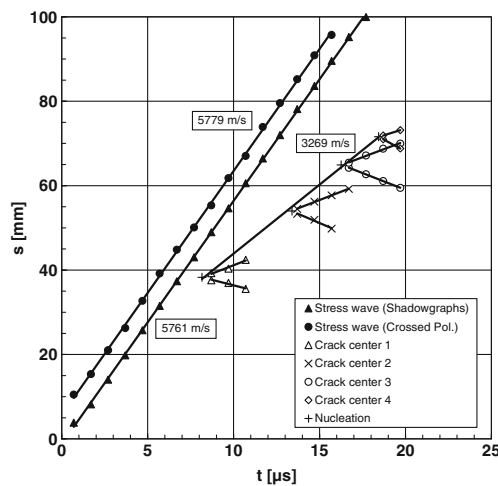


Fig. 29 Distance-time history of wave and damage propagation in Starphire™ glass depicted in Fig. 28(b)

After 23.7 μs (Fig. 31) the compressive stress wave has already reflected as a tensile wave from the rear edge of the glass plate in all three cases. The shadowgraphs illustrate that damage in the second glass layer is mainly due to the tensile wave and starts from the rear edge of the specimen. For the 5.08 mm PU interlayer only minimal damage was observed in the second glass layer. The wave and damage propagation in the glass laminates was analyzed and the distance-time history for the 5.08 mm PU bonding layer assembly is shown in Fig. 32.

The influence of two PU interlayers (2.54 mm thick) was also tested with glass laminate assemblies built from three plates of the dimensions $30 \times 100 \times 9.5$ mm. These results are shown in Fig. 33. Cylinder impactors at a velocity of about 400 m/s were used in this case. Careful examination of these photographs exhibit quite similar effects as seen for the two glass plate assemblies above. This figure presents a selection of four shadowgraphs and corresponding crossed polarizers photographs in the time interval from 6.7–24.7 μs after impact. The first layer of glass

was completely damaged within the first 15 μs . Damage can be seen in the second layer at 15.7 μs , when the first crack centers became visible which were initiated by the reflection of the compression wave at the interface between the second glass and the second bonding layer. No damage was observed in the third glass layer during the time interval of observation.

When the stress waves impact the interlayer one part is reflected while the other part is transmitted into the second glass layer. Due to the low acoustic impedance of the PU interlayer compared to the glass, the amplitude of the stress wave is attenuated considerably. The low wave velocity in the interlayer effects a time delay of 1.7 μs compared to the unperturbed propagation through the glass. The delay times measured in all tests were plotted in a delay time *versus* bonding layer thickness diagram (Fig. 34). Linear regression of the data yielded an average delay time of 0.33 $\mu\text{s}/\text{mm}$. This is in good agreement with the calculated value based on a longitudinal wave velocity $c_L = 5,770$ m/s for Starphire™ glass and $c_L \approx 2,000$ m/s for the polyurethane [49].

Total Damage Analysis

In addition to determining damage or crack velocity, an image analysis technique was developed to determine total evolved 2-D damage in plates as a function of time. Figure 35 shows the original gray-scale shadowgraph (left) and converted black and white image (right), used for damage analysis; the ratio of total converted black damaged area to the remaining undamaged white area was used for the estimation of the evolving 2-D damage. Although this is not exactly a representation of the total 3-D damage, in our opinion, it is a close estimate. This analysis was utilized to study the total 2-D damage evolution in a series of Starphire™ plates as shown in Fig. 36. It is our conclusion that the difference in damage evolution is the result of differences in the presence of internal defects. Note also that there seems to be significant differences in the damage evolution from the reflection tensile stresses at the back end of the plates.

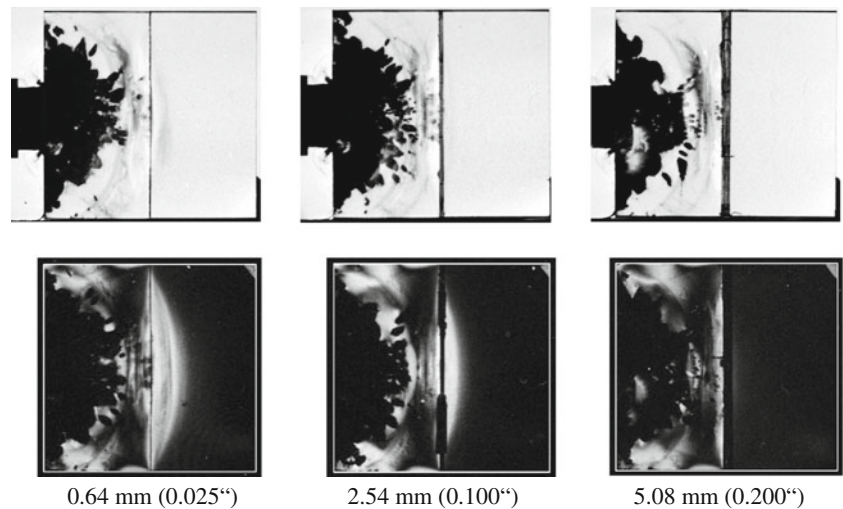
Table 3 Crack and damage velocities determined from EOI tests

Material	Longitudinal sound velocity (m/s)	Crack velocity (m/s)	Damage velocity (m/s)
Starphire (soda-lime glass)	≈ 5700 – 5800	1580	3270
Borofloat (borosilicate glass)	≈ 5500 – 5600	2034	4150
Fused Silica	≈ 6000	2400	5121
TRANSARM (glass ceramic)	≈ 6600	2151	4950
AION (polycrystalline ceramic)	≈ 10100 – 10300	4377	8381
Sapphire (cleavage cracks)	≈ 9000 – 10000	4800–5400	8434

Ultra-High Speed Photography of Impact Morphology

A ballistic test configuration (Fig. 37) has been used to record, with very high-speed photography, the impact event on a series of glasses and other ceramic materials [50,51]. The beginning of the projectile target interaction, crack propagation and the onset of the ejection of fragments were visualized with an ultra high-speed Shimadzu HPV camera, which allows recording a total number of 100 frames at a maximum rate of 10^6 frames per second. An armor piercing (AP) 7.62 mm \times

Fig. 30 Starphire™ laminates with polyurethane interlayers of different thickness after 10.7 μ s; top is unpolarized light, bottom is crossed polarized light; cylinder impactor at about 380 m/s



51 mm projectile, with steel core, and a total mass of 9.5 g was used for the tests. The steel cores had a mass of 3.7 g and a length of 23.5 mm. The tests were conducted at two different impact velocities, nominally 850 m/s and 1,100 m/s. The complete interaction of the projectile with the target should comprise three phases: dwell, ceramic penetration and backing penetration. An aluminum based material with a tensile strength 400 MPa and dimensions 200×200×25 mm was used as the backing material. The dimensions of the sample plates were approximately 90×90×5.7 mm and were bonded to the aluminum backing with 0.8 mm thick polyurethane glue. The sample plates were laterally surrounded by an aluminum frame with a small air gap of about 0.1 mm between the plate and the frame. The aluminum frame was utilized to keep the fragments in place that were not directly in the interaction zone. It did not serve as a confinement. The target was integrated into a target box, which allowed for an almost complete recovery and analysis of the ceramic

fragments as well as recording the complete initial stage of the impact process.

Figure 38 illustrates four selections of high speed photographs of impacts on AON, fused silica and a soda-lime glass. It is especially interesting to note that there was a significant difference in the propagating damage front for the AP projectile and the solid cylinder. Analysis of these morphologies and the resulting collected fragment distributions is currently underway.

Summary, Conclusions and Future Directions

The ultimate failure of structural ceramics in impact events is a function of the temporal and spatial interaction of the macro-stresses at the macro-, micro- and nano-structural scale, including elastic and inelastic (plastic) deformation, crack nucleation, damage evolution and resulting failure from the macro-scale (top down) and/or from the nano-scale (bottom up). In addition, there are important key

Fig. 31 Starphire™ laminates with polyurethane interlayers of different thickness after 23.7 μ s; top is unpolarized light, bottom is crossed polarized light; cylinder impactor at about 380 m/s

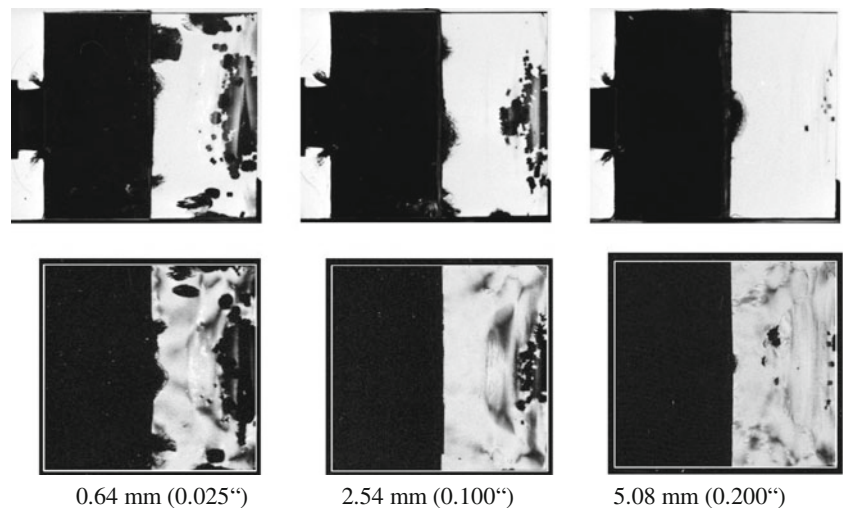
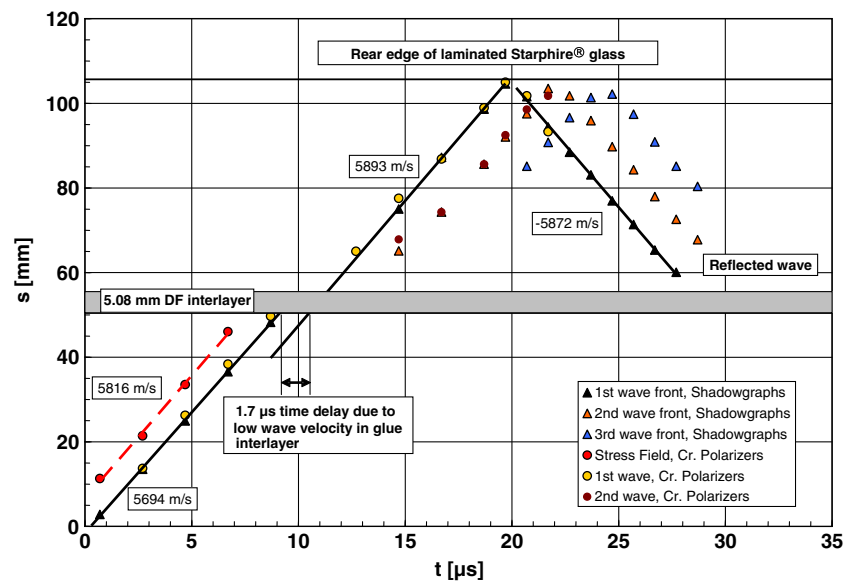


Fig. 32 Distance -time history of wave propagation in Starphire™ laminates with one 5.08 mm polyurethane interlayer



differences between typical quasi-static and dynamic stress environments that must be taken into consideration to interpret the results of dynamic impact events. Included among these are the volume of the stressed region, the apparent importance of a distribution of defects, the introduction of new deformation and failure mechanisms, the roles of the compression and shear waves and a complex mixed super stress state.

In order to accelerate the development of validated design and predictive performance models, a systematic series of dynamic mechanical testing techniques with real time, through thickness photography have been carried out on a series of transparent non-crystalline ceramics (glass), single crystal (sapphire) and polycrystalline ceramics (AION). Most brittle material models exclude defects, micro-cracking/cleavage, deformational twinning, ceramic-specific plasticity and failure mechanisms, among other

physics based phenomena. Inelastic deformation mechanisms of structural ceramics and glass in impact events, although seemingly important as energy absorption mechanisms, have not been sufficiently characterized. The Edge-on Impact (EOI) test coupled with a high-speed Cranz-Schardin film camera has been extensively used on a variety of monolithic and laminated glasses, AION and crystallographically controlled sapphire single crystals to visualize and quantify stress wave, crack and damage propagation. The influence of defects on glass and AION crack nucleation and damage evolution is apparent. Computational simulations have been carried out using ABAQUS Explicit to simulate the elastic wave propagation within the Edge-on Impact (EOI) experiments on AION. The simulations show that the major damage zone (failure wave) observed in the experiments basically tracks the shear stress dominated portion of the shock wave and that the compression wave is

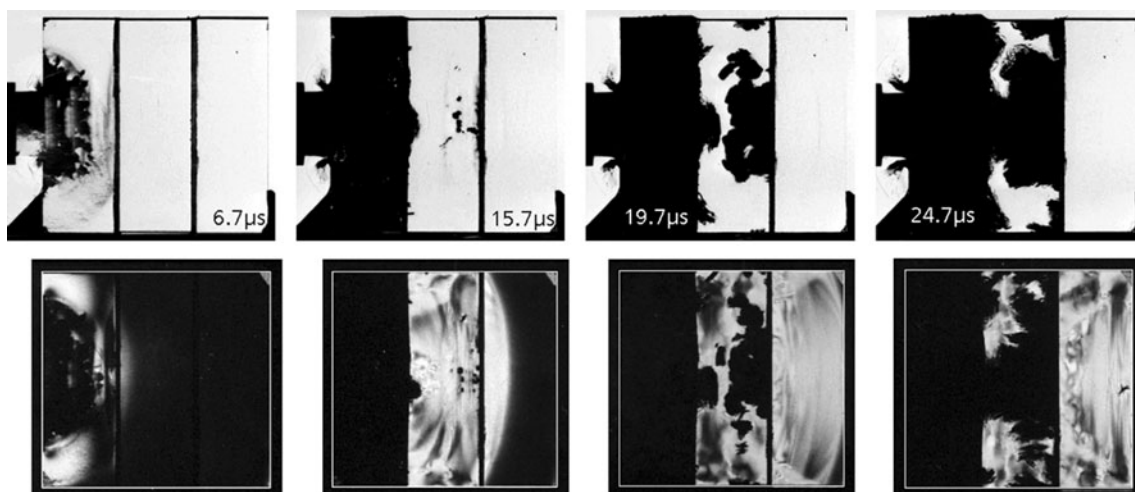


Fig. 33 Three layer Starphire™ target: 2×2.54 mm polyurethane interlayer; top is unpolarized light and bottom is polarized light

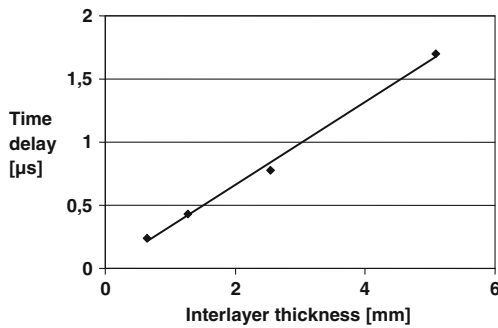


Fig. 34 Interlayer bonding delay time *versus* bonding layer thickness

parallel to the stress birefringent region and can “activate” defects. A modified Kolsky bar technique instrumented with a high speed digital camera has been utilized in an unconfined and confined test sample mode to examine the dynamic deformation and failure of AION undergoing uniaxial, high strain rate compression. Real time photography has clearly demonstrated the critical influence of defects and post mortem characterization of fragments resulting from these tests have revealed the presence of carbonaceous defects and of micro-deformational twinning and cleavage down to the nano-scale. In addition, the use of moderate confinement was shown to mitigate early material failure due to defects, increase maximum failure stress, and allowing “plasticity” mechanisms to be activated before ultimate failure.

In order to more clearly determine the mechanisms of deformation and failure in individual polycrystalline grains in the dynamic impact event, large single crystal plates of aluminum oxide (sapphire) in five crystallographically controlled orientations, were impacted in the EOI test configuration at about 400 m/s with both steel solid cylinders and spheres. Using the sphere impactors it is very clear that the various sapphire cleavage planes can have significant influence on the cracking morphologies; with the greater weight cylinders they are not quite as influential. It is our conclusion that the morphology of the damage front will be controlled by a competition between the available impact energy to create a massive undifferentiated damage front

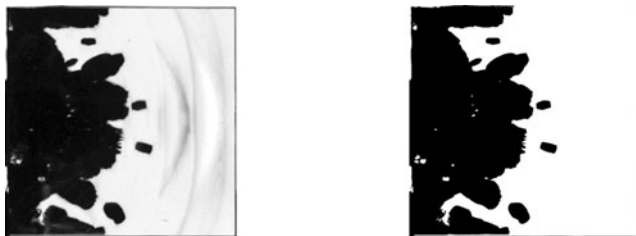


Fig. 35 Image analysis of total damage as a function of time. Comparison of original gray-scale shadowgraph (*left*) and converted black and white picture (*right*), used for damage analysis. In addition to measuring damage or crack velocity, determined total evolved damage in plate (2-D) as a function of time

with the energy to have the damage controlled by the available properly oriented cleavage planes. For certain levels of energy deposition, the critical resolved shear stress (Schmid factor), which is a function of the angle between the loading direction and the cleavage plane, will control the ease of formation of cleavage controlled cracks/damage or undifferentiated damage zones. Therefore, in some sapphire plate orientations, damage will be dominated by cleavage and not in others. Post mortem characterization of fragments from the EOI sapphire tests clearly demonstrate that the fracture surfaces exhibit cleavage controlled fracture down to the nano-scale.

Extensive EOI tests have also been carried out on a series of monolithic and laminated glass assemblies. It is again very clear, as in the AION work, that defects have a significant effect on the nucleation of cracks that precede and influence the main damage front. A more detailed damage analysis technique used on Starphire™ shows that the total 2D damage evolution can be significantly different in a series of different samples, seemingly controlled by the variability of defects. In this same series of experiments the damage resulting from the back reflection tensile stress is quite clear and significant. Testing was also carried out on both two layer and three layer glass laminates bonded together by a polyurethane glue. From these tests the major contribution of the tensile stress nucleated damage resulting from the back face reflection of the compression wave is apparent. In addition, the extremely complex nature of the effect of the bonding layers on the speed and morphology of the transmitted compression wave is also quite pronounced. In another series of tests on two layer laminates, the effect of different thicknesses of the bonding layer was determined. Using the polyurethane glue, the average time delay of the compression wave was 0.33 μs/mm of glue.

Important crack and damage front velocity data, that can be used to validate computer simulations of dynamic impact events, have been determined on monolithic and glass laminates, polycrystalline AION and single crystal sapphire materials using the EOI test configuration.

Finally, a brief summary of work using ultra-high-speed photography of the impact of conventional projectiles on glass and AION was presented. These experimental results will be absolutely critical to help evolve and validate existing models used in computer codes to simulate the impact performance of brittle materials. Work is currently underway to determine the velocities of the radial cracks, damage zones (failure waves) and the size distributions of the resulting fragments.

As discussed above, the experimental research activities, like the ones described in this paper, will be critical for the development of validated multi-scale modeling capabilities to accelerate the ability to design new materials and material

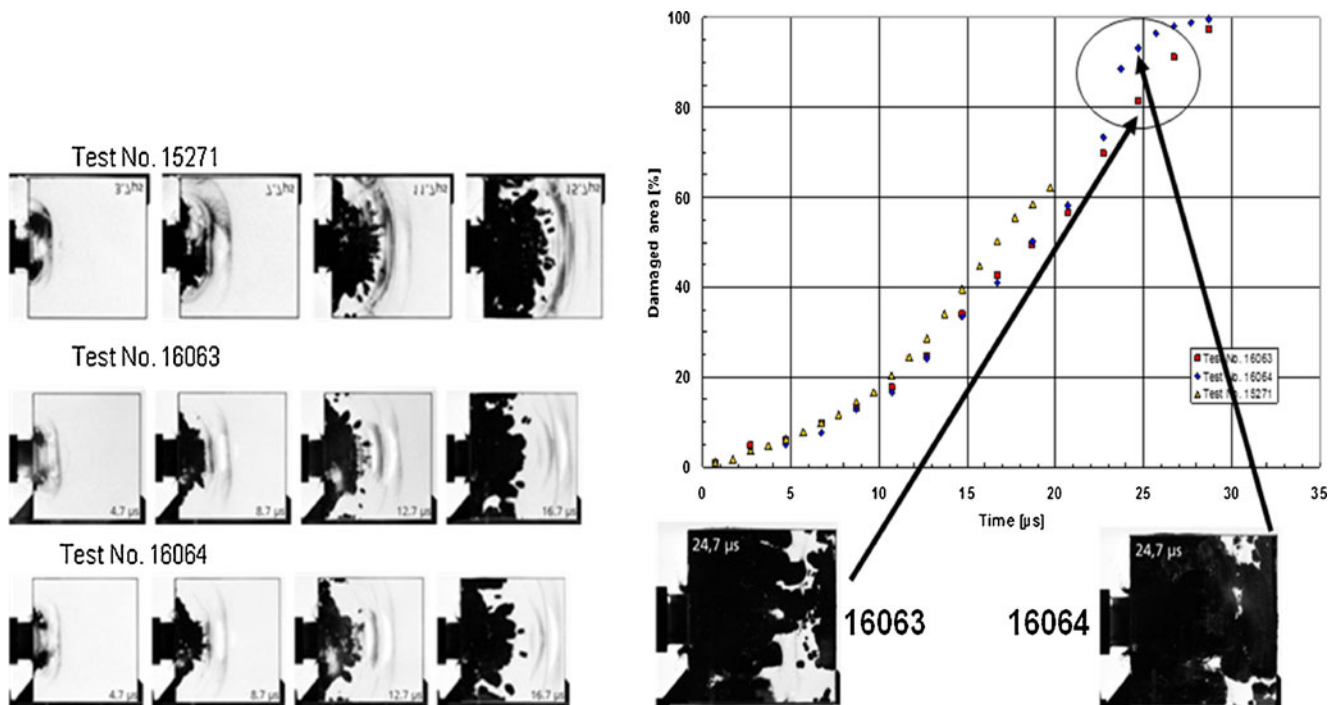
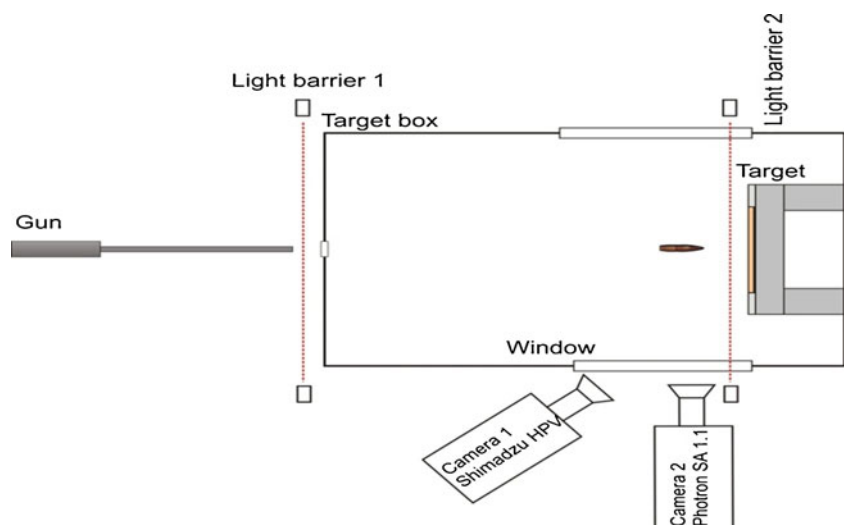


Fig. 36 Three baseline tests on three starphire™ samples with cylinders at about 400 m/s

systems (protection materials by design) and to predict performance. The work described here used real time photographic interrogation techniques of the impact events with only mechanisms visible with these techniques being observed. In addition, only post mortem characterization of resulting damaged material was carried out. Efforts must be initiated to use other real time interrogation/characterization techniques that can determine the operative mechanisms at relevant time and dimensional scales. Recently, multi-scale modeling efforts have been initiated on both glass and AlON at the U.S. Army Research Laboratory [52,53].

In addition, a new initiative by the U.S. Army Research Laboratory to create a Collaborative Research Alliance (CRA) on Materials in Extreme Dynamic Environments (MEDE) is currently being started. Using a “Protection Materials by Design Approach” the overall program will include both extramural and in-house activities in a collaborative mode. The program is based on a multiscale materials approach and will include major efforts on metals, ceramics, polymers and composites focusing on the following cross cutting thrusts: multiscale modeling and simulation, methods for

Fig. 37 Schematic of ballistic test configuration



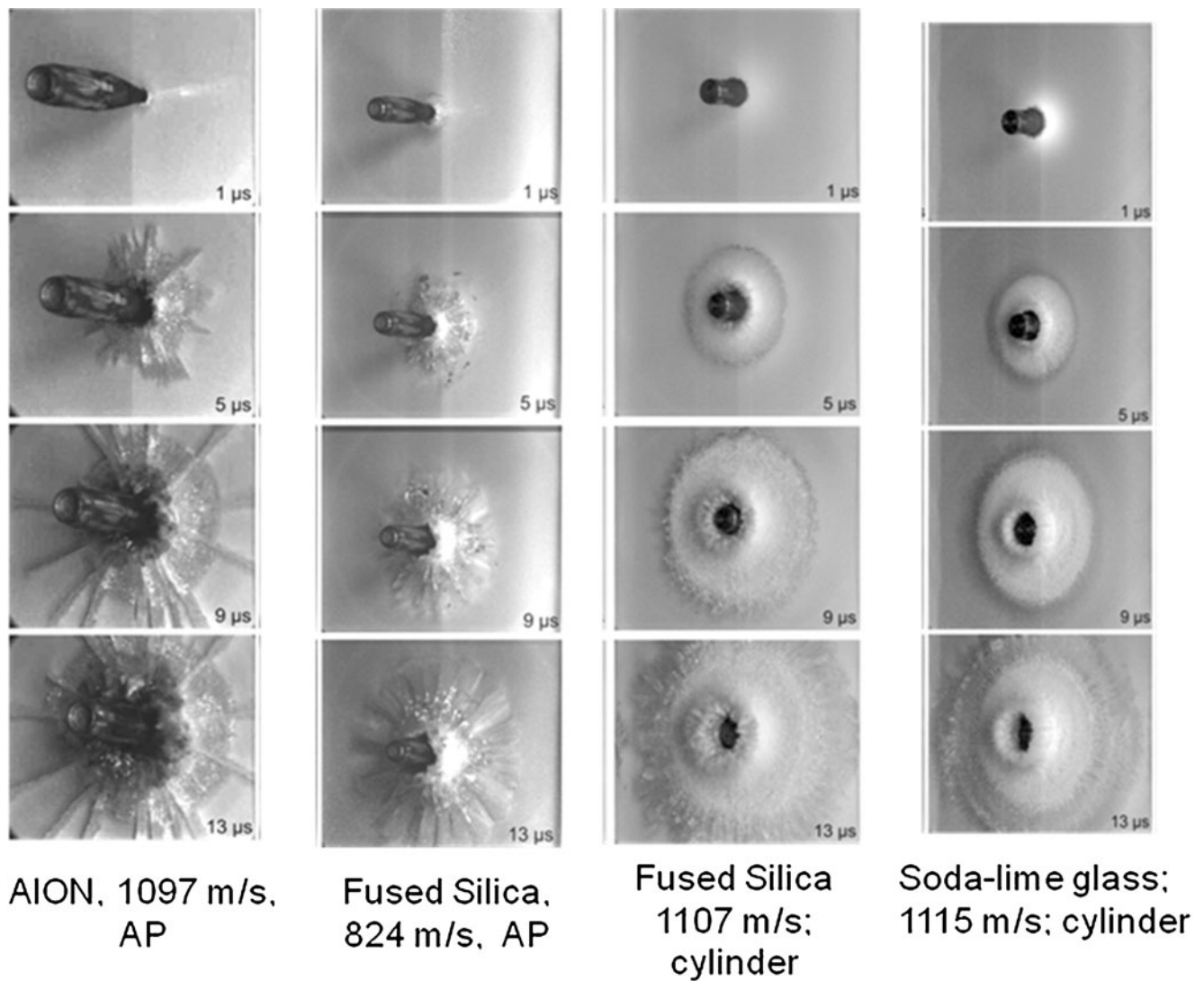


Fig. 38 Selection of a series of ultra-high-speed photographs, at the same times, of impacts into glass and AION plates using 7.62 mm armor piercing (AP) and solid cylinder projectiles

bridging the computational scales, real time experimental and interrogation techniques, synthesis and processing and the determination and use of material characteristics (phase, microstructure and defects) and property metrics. The overall objective is to evolve the capability to design, optimize, and fabricate lightweight protection material systems exhibiting revolutionary performance by advancing the fundamental understanding of materials in relevant high strain rate and high stress regimes.

Acknowledgments We want to especially acknowledge the support of Dr. Douglas W. Templeton, US Army TARDEC, Warren, Michigan, for his support in the early years of the efforts at the Ernst Mach Institute. We would also like to thank Martin Hunzinger of the Fraunhofer Institute for High-Speed Dynamics, Ernst-Mach-Institute (EMI) for his assistance with the fragmentation experiments.

References

1. Patel P, Gilde G, Dehmer P, McCauley JW (2000) Transparent armor. AMPTIAC 4(3):1–13
2. Wax SG, McCauley JW, Logan KV, Fehrenbacher LL, Gilde G (1998) DARPA/ARL/ARO transparent armor materials workshop. TA&T Inc., Annapolis
3. Sands JM, McCauley JW (2008) 50th Anniversary Celebration: 46th Sagamore Army Materials Research Conference on Advances and Needs in Multi-spectral Transparent Materials Technology. ARL-SR-0164
4. Opportunities in Protection Materials Science and Technology for Future Army Applications (2011) The National Academies Press, Washington, D.C.
5. Graff KF (1991) Wave motion in elastic solids, Dover Publications
6. Senf H, Straßburger E, Rothenhäusler E (1994) Stress wave induced damage and fracture in impacted glasses. J Phys IV 4:741–746, C8
7. Strassburger E (2004) Visualization of impact damage in ceramics using the edge-on impact technique. Int J Appl Ceram Technol 1 (3):235–242

8. Straßburger E, Steinhauser MO (2008) High-speed photographic study of wave propagation and impact damage in transparent laminates, ARL-CR-605
9. McCauley JW, Patel P, Chen MW, Gilde G, Strassburger E, Paliwal B, Ramesh KT, Dandekar DP (2009) AION: a brief history of its emergence and evolution. *J Eur Ceram Soc* 29:223–236
10. Krell A, Bales A (2010) Grain size dependent hardness of transparent magnesium aluminate spinel, IJACT, Published on line, 22 October 2010
11. Krell A, Hutzler T, Klimke J (2009) Advanced spinel and Sub-micron Al₂O₃ for transparent armor applications. *J Eur Ceram Soc* 29:275–281
12. Nie X, Wright JC, Chen WW, Fehrenbacher L, Vesnovky I (2011) Rate effects on the mechanical response on magnesium aluminate spinel. *Mater Sci Eng A* 528:5088–5095
13. Haney E, Subhash G (2011) Rate sensitive indentation of a coarse grained magnesium aluminate spinel. *J Am Ceram Soc* 94(11):3960–3966
14. McCauley JW, Patel P (2012) Evaluation of IKTS Transparent Polycrystalline Magnesium Aluminate Spinel (MgAl₂O₄), in preparation
15. Strassburger E, Hunzinger M, Patel P, McCauley JW (2011) Analysis of the fragmentation of spinel under ballistic impact, Proceedings of the 35th International Conference and Exposition on Advanced Ceramics & Composites, January 23–28 2011, Daytona Beach, Florida
16. Strassburger E, Hunzinger M, Patel P, McCauley JW (2013) Analysis of the fragmentation of AION and Spinel under ballistic impact, to be presented at the 27th International Symposium on Ballistics, 22–26 April 2013 Freiburg, Germany
17. Haney EJ, Subhash G (2012) Edge-on-impact response of a coarse-grained magnesium aluminate spinel rod. *Int J Impact Eng* 40–41:26–34
18. Strassburger E, Patel P, McCauley JW, Templeton DW (2005) Visualization of wave propagation and impact damage in a polycrystalline transparent ceramic – AION. Proceedings of 22nd International Symposium on Ballistics, Vancouver, BC, Canada
19. Strassburger E (2006) High-speed photographic study of wave propagation and impact damage in transparent Aluminum Oxynitride (AION). ARL-CR-579
20. Chen MW, McCauley JW, Hemker K (2003) Shock-induced localized amorphization in B₄C. *Science* 299:1563–1566
21. Strassburger E, Hunzinger M, McCauley JW, Patel P (2010) Experimental methods for characterization and evaluation of transparent armor materials. Proceedings of the 34th International Conference and Exposition on Advanced Ceramics & Composites, Daytona Beach, Florida, CESP, V. 31, 183–198
22. Grinfeld MA, McCauley JW, Schoenfel SE, Wright TW (2007) Failure pattern formation in brittle ceramics and glasses, 23rd International Symposium on Ballistics, Tarragona, Spain
23. LaSalvia JC, McCauley JW (2010) Inelastic deformation mechanisms and damage in structural ceramics subjected to high-velocity impact. *IJACT* 7(5):595–605
24. Strassburger E, Patel P, McCauley JW, Kovalchick C, Ramesh KT, Templeton DW (2006) High-speed transmission shadowgraphic and dynamic photoelasticity study of stress wave and impact damage propagation in transparent materials and laminates using the Edge-on Impact (EOI) Method. Proceedings of the 25th Army Science Conference, Orlando, FL, J. A. Parmentola and A. M. Rajendran, eds., Tech Science Press, 227–233. (ARL-RP-203, March 2008)
25. Paliwal B, Ramesh KT, McCauley JW (2006) Direct observation of the dynamic compressive failure of a transparent polycrystalline ceramic (AION). *J Am Ceram Soc* 89(7):2128–2133
26. Paliwal B, Ramesh KT, McCauley JW, Chen MW (2008) Dynamic compressive failure in AION under controlled planar confinement. *J ACerS* 91(11):3619–3629
27. Guo JJ, Wang K, Fujita T, McCauley JW, Singh JP, Chen MW (2011) Nanoindentation characterization of deformation and failure of aluminum oxynitride. *Acta Mater* 59:1671–1679
28. Wilantewicz TE (2010) Failure behavior of glass and Aluminum Oxynitride (AION) Tiles Under Spherical Indenters, ARL-TR-5180
29. Muller A (2011) Identification of deformation and failure mechanisms in armor ceramics, Ph.D. thesis, The Pennsylvania State University
30. Dandekar DP, McCauley JW, Bourne NK, Chen MW (2008) Global mechanical response and its relation to deformation and failure modes at various length scales under shock impact in Alumina AD995 armor ceramic, ARL-RP-202, March 2008
31. Chen MW, McCauley JW, Dandekar DP, Bourne NK (2006) Dynamic plasticity and failure of high-purity alumina under shock loading. *Nat Mater* 5:614–618
32. Bourne NK, Millet JCF, Chen MW, Dandekar DP, McCauley JW (2007) On the hugoniot elastic limit in polycrystalline alumina. *J Appl Phys* 102:073514
33. Haney EJ, Subhash G (2011) Static and dynamic response of basal and prism plane sapphire. *J Eur Ceram Soc* 31:1713–1721
34. Haney EJ, Subhash G (2011) Analysis of interacting cracks due to sequential indentation on sapphire. *Acta Mater* 59:3528–3536
35. Winkler S (1993) Experimental investigation of wave and fracture phenomena in impacted ceramics; final report 'experiments on sapphire. Fraunhofer-Institut für Werkstoffmechanik, Freiburg, IWM Report T 8/93
36. Senf H, Winkler S (1997) Experimental Investigation of Wave and Fracture Phenomena in Impacted Ceramics: Sapphire. ARL-CR-310
37. Strassburger E, Patel P, McCauley JW (2011) Visualization and analysis of impact damage in sapphire. ARL-RP-345
38. Winey JM, Gupta YM (2001) r-axis sound speed and elastic properties of sapphire single crystals. *J Appl Phys* 90(6):3109–3111
39. Bradt R (1997) Cleavage of ceramic and mineral single crystals. George R. Irwin Symposium, Proceedings of a symposium at the TMS Meeting, Indianapolis, Indiana, 355–365
40. Iwasa M, Bradt RC (1983) Fracture toughness of single-crystal alumina. *Advances in ceramics*, Vol. 10, Proceedings of an International Symposium Held at the Mass. Inst. Tech, Cambridge, MA, 767–779
41. Shappel MD (1936) Cleavage of ionic minerals. *Am Mineral* 21(2):75–102
42. Mackrodt WC (1989) Atomistic simulation of the surfaces of oxides. *J Chem Soc Faraday Trans* 85(5):541–554
43. Tasker PW (1983) Surfaces of magnesia and alumina, WD Kingery, ed., *Adv. in Ceramics*, vol. 10, p. 176–189
44. Hartman P (1989) The effect of surface relaxation on crystal habit – cases of corundum (alpha-Al₂O₃) and hematite (alpha-Fe₂O₃). *J Cryst Growth* 96:667–672
45. Clayton J (2009) Finite deformations by elasticity, slip, and twinning: atomistic considerations, continuum modeling, and application to ceramic crystals. ARL-RP-244
46. Strassburger E, Patel P, McCauley JW, Templeton DW, Varshneya A (2008) High-speed photographic study of wave propagation and impact damage in novel glass laminates. Proc. of the 24th Int. Symposium on Ballistics, 548–555
47. Strassburger E, Patel P, McCauley JW, Templeton DW (2007) Wave propagation and impact damage in transparent laminates. 23rd International Symposium on Ballistics, Tarragona, Spain
48. Strassburger E (2010) Stress wave and damage propagation in transparent laminates at elevated temperatures. ARL-CR-639
49. Gupta YM (1984) High strain-rate shear deformation of a polyurethane elastomer subjected to impact loading. *Polym Eng Sci* 24:11
50. Strassburger E, Hunzinger M, Bauer S (2011) Complementary edge-on impact tests and analysis of the fragmentation of spinel.

- Report E 11/11, Fraunhofer Institut für Kurzzeitdynamik (EMI), Kanderndorf, Germany
51. Strassburger E, Hunzinger M, Bauer S (2011) Analysis of the fragmentation of AlON and bi-modal grain sized Spinel. Report E 39/11, Fraunhofer Institut für Kurzzeitdynamik (EMI), Kanderndorf, Germany
52. Gazonas GA, McCauley JW, Batyrev IG, Casem D, Clayton JD, Dandekar DP, Kraft R, Love BM, Rice BM, Schuster BE, Weingarten NS (2010) Multiscale modeling of armor ceramics: Focus on AlON. ARL-RP-337; Sept. 2011. A reprint from Proceedings of the 27th Army Science Conference, Orlando, FL
53. Gazonas GA, McCauley JW, Batyrev IG, Becker RC, Izvekov S, Patel P, Rice BM, Schuster BE, Weingarten NS, Wildman RA (2012) Multiscale modeling of non-crystalline ceramics (Glass): ARL-MR-080

1 DEFENSE TECHNICAL
(PDF) INFORMATION CTR
DTIC OCA

2 DIRECTOR
(PDF) US ARMY RESEARCH LAB
RDRL CIO LL
IMAL HRA MAIL & RECORDS MGMT

1 GOVT PRINTG OFC
(PDF) A MALHOTRA

ABERDEEN PROVING GROUND

49 DIR USARL
(7 HC, RDRL CIH C
42 PDF) P CHUNG
D GROVE
J KNAP
RDRL WM
P BAKER
B FORCH
J MCCAULEY (6 HC)
P PLOSTINS
RDRL WML B
I BATYREV
B RICE
D TAYLOR
N WEINGARTEN
RDRL WML H
B SCHUSTER
RDRL WMM
J BEATTY
R DOWDING
J ZABINSKI
RDRL WMM B
G GAZONAS
RDRL WMM E
C HILTON
S KILCZEWSKI
J LASALVIA
P PATEL
J SINGH
J SWAB
RDRL WMP
S SCHOENFELD
RDRL WMP B
C HOPPEL
D POWELL
S SATAPATHY
M SCHEIDLER
T WEERASOORIYA
RDRL WMP C
R BECKER
S BILYK

T BJERKE
D CASEM
J CLAYTON (1 HC)
D DANDEKAR
M GREENFIELD
R LEAVY
M RAFTENBERG
S SEGLETES
C WILLIAMS
RDRL WMP D
R DONEY
RDRL WMP E
S BARTUS
RDRL WMP F
N GNIAZDOWSKI
RDRL WMS
M VANLANDINGHAM